BREAKING THE CYCLE: THE RISE AND FALL OF CONVERSION CYCLE LIMITED THREE-WAVE MIXING

A Dissertation

Presented to the Faculty of the Graduate School

of Cornell University

in Partial Fulfillment of the Requirements for the Degree of

Doctor of Philosophy

by

Noah Rowe Flemens

August 2022

BREAKING THE CYCLE: THE RISE AND FALL OF CONVERSION CYCLE LIMITED THREE-WAVE MIXING

Noah Rowe Flemens, Ph.D.

Cornell University 2022

The cyclic exchange of energy between the pump, signal, and idler fields that characterizes optical parametric amplification (OPA) places a fundamental limitation on efficiency for Gaussian-shaped beam and pulse profiles typical of real laser sources. This is because the intensity dependent conversion period of OPA results in asynchronous conversion across the spatiotemporal intensity profiles of the mixing laser fields. We introduce a new method for achieving efficient OPA by using simultaneously phase-matched idler second harmonic generation (SHG) to act as an effective loss-channel for idler photons. The dynamics are characterized by damped conversion cycles, leading to asymptotic conversion of the pump and idler to the signal and idler second harmonic fields at all points in transverse space and time. We develop a damped Duffing oscillator model that unifies the description of conventional OPA with OPAs that use linear absorption [60, 23, 96, 55, 61] or SHG [31] to remove idler photons and enhance efficiency. An experimental demonstration in a $CdSiP_2$-based device enables 68% pump depletion with 44% pump to signal energy conversion efficiency–a several fold increase over conventional OPA efficiency.

We then show that SHG can replace loss to induce non-Hermitian features such as regions of broken and unbroken PT-symmetric phase demarcated by an exceptional point in three-wave mixing nonlinear interactions. This enables a new paradigm where the behavior associated with the PT-symmetric phase

of a non-Hermitian subsystem can be used to control the containing Hermitian system through the coherent couplings. These findings suggest a new approach for the engineering of dynamics where energy recovery and sustainability are of importance in photonics and laser science.

Finally, we demonstrate self-dispersion managed adiabatic difference frequency generation (ADFG). While ADFG has been demonstrated to produce single-cycle pulses in the mid-IR [47], this is not without the challenge of implementing a complicated dispersion management scheme to compensate for the complex dispersion imparted by the device. We engineer and characterize an aperiodically poled $LiNbO_3$ device that generates an octave-spanning bandwidth in the mid-IR (2-4 μm) that imparts no net dispersion to the generated light.

BIOGRAPHICAL SKETCH

Noah Rowe Flemens was a late bloomer in his passion for science. After exhausting the intro-course offerings at his local community college, he enrolled in calculus. The Bunsen burner was lit. He transferred to UC Berkeley where he received B.A.'s in math and physics. He received a M.S from Cornell University in 2017 where he is currently pursuing a Ph.D. in applied physics. His research interests focus on the development of novel and efficient nonlinear optical technologies.

To my friends and family who have listened supportively throughout the years when I ramble on about science.

ACKNOWLEDGEMENTS

I acknowledge my labmates, Dr. Dylan Heberle, Dr. Xiaoyue Ding, Dr. Wei-Zung Chang, Jiaoyang Zheng, and Oscar Jaramillo for their many years of support. I thank Dr. Dylan Heberle in particular, who in the early years of our lab, was my comrade in arms in our battle for laser stability. I would also like to thank the multitude of undergrads, Devin Dean, Nick Swenson, Yazhi Fan, Derrick Lin, David Chaparro, Cecilia Chen, Matthew Herbrand, Duncan McKeen, Ryan Kishore, and Nuno Mendes Castanheira who helped us investigate new nonlinear optical phenomena, build our lab, and plan experiments over the years. In addition, I thank Dr. Walter Fu, Dr. Logan Wright, Dr. Frank Wise, Dr. Farhan Rana, and Dr. Francesco Monticone for years of insightful discussions.

I express my deepest gratitude to my advisor, Dr. Jeffrey Moses, for being a well of patience and encouragement. Our every conversation left me motivated and inspired.

TABLE OF CONTENTS

LIST OF TABLES

LIST OF FIGURES

CHAPTER 1

INTRODUCTION

Sixty years since the identification of nonlinear three-wave mixing as a means for amplification of light [45, 49, 2, 1], optical parametric amplification (OPA) continues to be a major research area. More recently, a rise in research activity was fueled by the emergence of Ti:sapphire and Yb-doped solid-state laser amplifiers that can be used as powerful OPA pump sources in the near-infrared, giving rise to significant advances to meet the needs of nonlinear spectroscopy, nonlinear imaging, strong-field and relativistic optics applications [10, 72, 21, 94, 92, 26, 62, 32]. Throughout the wide frequency range of sources, new records are regularly set for pulse duration, intensity, pulse energy and average power. However, poor amplifier efficiency is usually a limiting factor.

Poor efficiency is the result of two problems. First is the energy lost to an undesired wave due to the splitting of pump energy between signal and idler photons (energy lost = $\omega_{\text{idler}}/\omega_{\text{pump}}$ or $\omega_{\text{signal}}/\omega_{\text{pump}}$, depending on whether the seeded signal or unseeded idler wave is desired) – the so-called *quantum defect*. This problem is especially severe when a transfer of energy to a much lower frequency is required.

Second is the problem of spatiotemporally asynchronous conversion of pump photons, which is usually discussed in terms of an intensity-dependent exponential gain coefficient, $G \propto \exp(gz)$, where g is proportional to the square-root of the local pump intensity, which varies in time and space. However, the root of this problem is the cyclic flow of energy between waves – known as conversion-back-conversion cycles – and the cycle period's dependence on the pump intensity (Fig. 1.1) - a problem identified at least four decades ago

and investigated in several works [69, 6, 70]. For conversion of all available pump photons to the signal and idler frequencies, all spatiotemporal coordinates of interacting waves must share a common length at which the peak of the conversion cycle occurs, since only one crystal length can be chosen. This cannot occur for free-space OPA with bell-shaped beam and pulse profiles. The maximum photon conversion efficiency can be estimated analytically via the exact Jacobi elliptic function solutions of the process (neglecting dispersion and diffraction)[70]. When each pump profile is Gaussian and the signal wavelength is seeded uniformly in space and time (as if by a much longer seed pulse and wider seed beam), only 20% of pump photons are converted for an amplifier with a peak gain of 100. When the peak gain is 10^5, the number drops to 10%. These poor numbers, combined with the quantum defect, underlie the many published reports of energy conversion from pump to signal in the 5-20% range for $\omega_s > \omega_i$ and sub-percent to few percent when $\omega_s \ll \omega_i$. Similar efficiencies are obtained for the unseeded wave (i.e., the idler). The roughly one to two order of magnitude drop in energy from pump to signal and idler beams greatly increases the cost of OPA systems while limiting their power and thus the scientific or industrial applications made accessible by them.

To mitigate the problem, pulse and beam shaping have been proposed. Uniform pump and seed profiles eliminate the asynchronous spatiotemporal conversion problem, and flattop-profile pump shaping in one or more transverse dimensions has been implemented successfully in some systems, e.g., [4, 33]. Idealized conformal profiles [6, 70] have been proposed for maximizing energy conversion and amplification bandwidth, as well as passive methods for achieving conformal-like profiles, such as cascaded extraction [9] and pump pulse reshaping caused by spatiotemporal variations in impedance matching within an

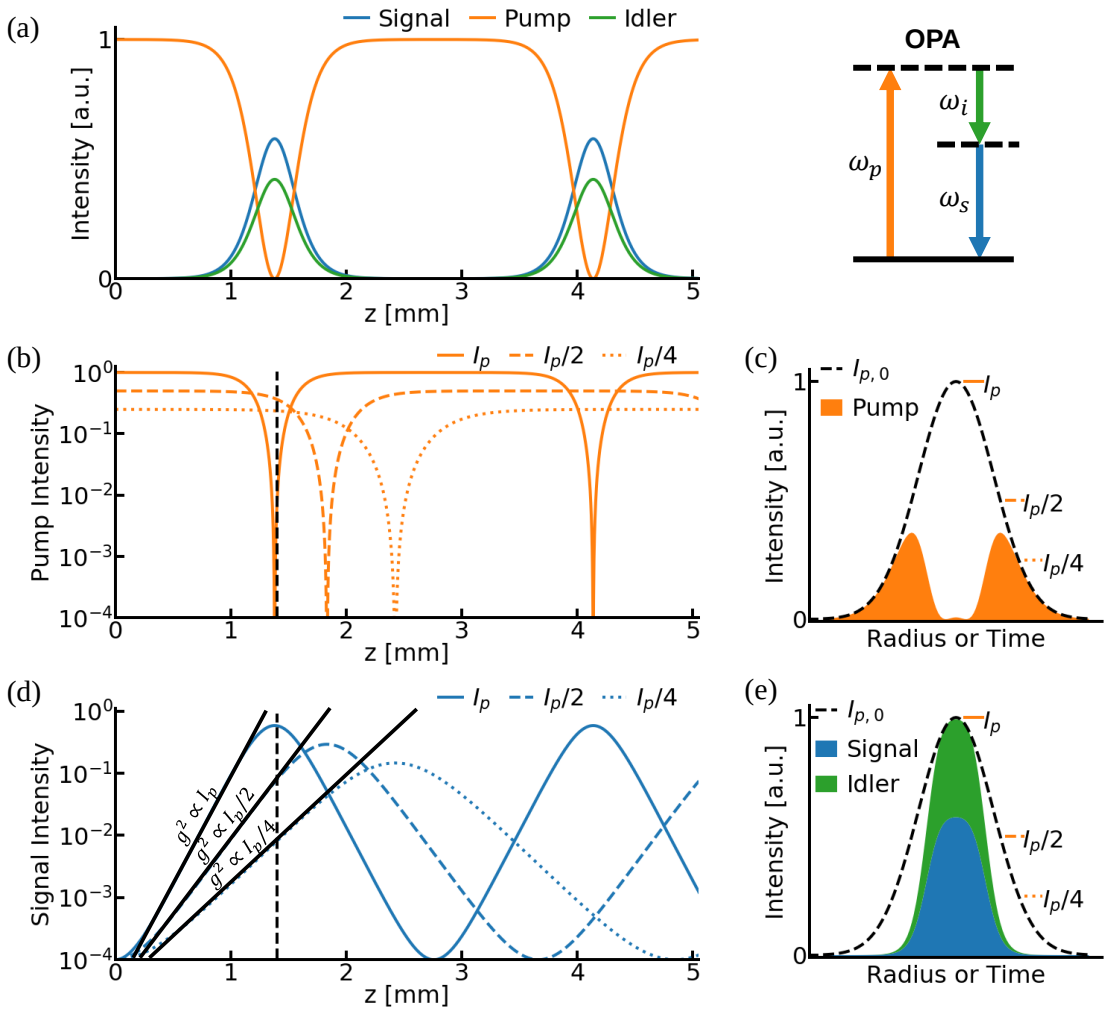

Figure 1.1: In OPA, conversion of pump to signal and idler occurs cyclically (a) with pump depletion (b) having a strong dependence on local pump intensity due to the variation in cycle period. (c) At the optimal crystal length for a Gaussian spatiotemporal pump intensity profile (gray dashed line in (b)), the profile wings remain mostly undepleted in both space and time, a severe source of OPA inefficiency. Similarly, the signal gain coefficient (d) depends on the pump-intensity-dependent conversion cycle period, leading to gain narrowing in the signal and idler spatiotemporal profiles that reflects the inefficient extraction of power from the pump (e).

enhancement cavity [88, 87]. For most applications, however, the pump shaping is a challenge, either due to implementation complexity, or because the pulse shaping itself imparts too significant a loss to be practical for boosting efficiency.

Alternatively, recent works have focused on forcing evolution dynamics with suppressed back-conversion. Adiabatic frequency conversion [90, 64], which uses the nonlinear optical analog of rapid adiabatic passage via a swept phase-matching condition, is one such method. Adiabatic frequency conversion can achieve full photon population inversion in the presence of a strong wave in sum- and difference-frequency generation and four-wave mixing Bragg scattering [89, 71, 8, 5, 19]. However, in OPA, where the aim is to deplete the strong pump wave, there is still a bandwidth-efficiency trade-off [76, 78]. Thus, while efficiency gains have been observed in adiabatic OPA processes, the technique is used more widely to extend bandwidth[12, 37, 38, 67, 66, 83, 64]. Recently, dissipative variants of OPA were proposed – named quasi-parametric amplification (QPA) or dissipative OPA – in which the introduction of material losses to the idler wave or spatial separation of the idler damps out conversion cycles by preventing the recombination of signal and idler photons that returns energy to the pump [60, 23, 96, 55, 61]. In one such work, the addition of a samarium dopant to a bulk yttrium calcium oxyborate crystal allowed 41% energy conversion efficiency from pump to signal [60], with conversion cycles largely damped across the majority of the spatiotemporal profile, thus making the asynchronicity of the conversion cycle irrelevant. These promising findings provide hope for the development of widely applicable solutions to the spatiotemporally inhomogeneous conversion problem in OPA based on back-conversion suppression, and thus for achieving energy efficiency approaching the quantum defect limit. However, the reliance on a material resonance to inhibit back-conversion

greatly restricts the wavelengths where this process is possible and introduces issues of thermal loading when scaling to high average powers.

In Chapter 2, we will explore a new method that overcomes the conversion cycle efficiency limitation by shaping OPA dynamics through purely parametric means. This new technique is called second harmonic amplification (SHA), wherein second harmonic generation (SHG) is used as a nonlinear loss channel for the OPA idler wavelength. We show how SHG can be used to unidirectionally displace photons from one field to another and how this leads to loss-like behavior, yet all of the displaced energy is preserved in a coherent co-propagating field. We then derive a general damped Duffing oscillator equation that describes a family of OPAs including conventional OPA, QPA, and SHA. This enables the use of a precisely defined damping parameter that depends on the relative strength of the OPA and SHG processes to determine whether the dynamics of the system will adhere to underdamped, critically damped, or overdamped oscillatory behavior.

To demonstrate the effectiveness of SHA for enhancing OPA efficiency, we perform 2+1D spatiotemporal Fourier split-step simulations in a realistic device using $CdSiP_2$ as the nonlinear medium where a 2.05 μm pump beam amplifies a 3 μm signal. We observe 80% pump energy depletion with 55% of that energy transferring to the signal field. Next, a device employing a quasi-phase matched $LiNbO_3$ superlattice structure is simulated. A 1.03 μm pump amplifies a 120-fs 1.63 μm signal with 44% pump to signal energy conversion. Finally, we discuss the effects of phase mismatch on the process and show how it can limit on conversion efficiency.

Chapter 3 details the first experimental demonstration of the simultaneous

OPA+SHG concept. This experiment uses a 2.19 μm pump to amplify a 3.39 μm signal in a CSP device, generating a 3.1 μm idler SH in the process. Measurements of the pump to signal energy efficiency show monotonic growth of the signal energy, reaching as high as 44% with the full available pump power. These results are a dramatic demonstration of how the damped oscillatory dynamics induced by SHG can lead to a several fold increase in efficiency over the case of conventional OPA.

Several other measurements are discussed that characterize and verify the performance of the device. Characterization includes the spectral, intensity, and beam measurements. To verify the dynamics match the theoretically predicted damped oscillations, the pump fluence is measured for increasing amounts of amplification. Damped conversion cycles are clearly seen with concentric rings of depletion forming in the residual pump fluence as the input pump power is increased. This is a first demonstration of this loss like behavior due to SHG.

Chapter 4 generalizes the use of second harmonic generation as a nonlinear loss channel for any non-degenerate three-wave mixing (TWM) process. Through a coupled mode analysis, we identify the existence of an exceptional point which demarcates regions of broken and unbroken PT-symmetric phase in a non-hermitian 2-mode subsystem of the Hermitian 4-mode TWM+SHG system. While there have been many promising recent efforts to circumvent the use of incoherent gain and loss to generate exceptional points, this is the first demonstration of this phenomenon without making linearizing or adiabatic following approximations. This allows us to study the a new phenomenon where the PT-symmetry phase of the non-Hermitian subystem drives the behavior of the full energy conserving Hermitian system.

Chapter 5 starts with an investigation of the dispersion properties of adiabatic frequency conversion (AFC). AFC addresses a different limitation imposed by conversion cycles known as the bandwidth-efficiency trade-off [64]. It mitigates this limitation by slowly varying the phase mismatch across the length of a quasi-phase matched nonlinear device. This results in every frequency in the desired bandwidth experiencing localized phase matching at different propagation coordinates within the device. It has been experimentally demonstrated that this can enable a linear transfer of amplitude and phase from input to output for octave-spanning bandwidths with an efficiency that grows monotonically with the pumping field [47].

However, the locality of the frequency conversion leads to a complicated dispersion profile for the device if left uncompensated. We show how to engineer a device that cancels its own material dispersion using the locality of conversion for each frequency in an octave-spanning bandwidth. This enables transform limited 10-fs pulses in the near-IR to be transferred directly to 10-fs pulses in the mid-IR without additional dispersion compensation. We show an experimental demonstration in an aperiodically-poled LiNbO3 device for generating a 2-4 μm octave-spanning bandwidth with 15.9 fs pulse duration from 13.5 fs near-IR pulses with 70% conversion efficiency. Additionally, a new phase retrieval technique known as FROSt is used to confirm proper device functionality [54, 59].

[1]

[1]This chapter uses material from [31]

CHAPTER 2

EFFICIENT PARAMETRIC AMPLIFICATION VIA SIMULTANEOUS SECOND HARMONIC GENERATION

Here, we introduce a new back-conversion suppression approach for solving the OPA conversion efficiency problem that can work in ordinary bulk nonlinear media (Fig. 2.1). We find that the nonlinear evolution dynamics resulting from simultaneously phase-matched OPA and idler second harmonic generation (SHG) are those of a damped nonlinear oscillator (Fig. 2.2). This closed, conservative system, which we call second harmonic amplification (SHA), mimics the damped oscillatory behavior and convergence to a static steady state characteristic of OPA with linear loss (such as QPA). However, as the system is fully parametric there is no loss: all of the energy remains in coherent optical fields at the end of the device. To demonstrate the close similarity of dynamical behavior between SHA and QPA and their relationship to conventional OPA, we further introduce a Duffing oscillator model of parametric amplification that unifies the description of all three processes under a generalized theoretical framework.

To demonstrate the promise of the SHA approach to strongly boost OPA efficiency, we perform spatiotemporal pulse propagation analyses in implementations relevant to modern ultrafast laser systems with ordinary Gaussian intensity profiles: birefringent phase matching in cadmium silicon phosphide (CSP) is predicted to allow conversion of a 1-ps, 2-μm laser to 3-μm with 55% energy efficiency, corresponding to 80% pump depletion after 50 dB gain, and a readily manufacturable lithium niobate (LNB) quasi-phase matching (QPM) structure can amplify 180-fs, 1.63 μm signal pulses with 68% depletion of a 1-μm pump

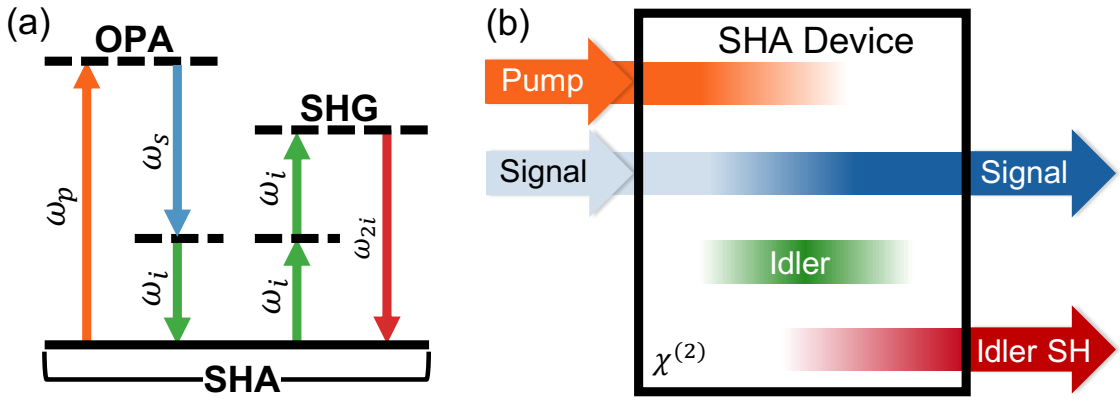

Figure 2.1: The second harmonic amplification (SHA) concept, consisting of simultaneous OPA and SHG of the idler. (a) Photon energy exchange diagram. (b) Schematic of the desired energy exchange within a device phase matched for both processes.

resulting in 44% energy conversion to the signal. In both cases, net unidirectional energy flow over the majority of the spatiotemporal extent of the interacting waves is observed, eliminating spatial and temporal gain narrowing, and with a several-fold improvement in conversion efficiency compared to the performance of conventional OPA. The SHA process thus appears to offer a solution to the longstanding problem of OPA inefficiency due to spatiotemporally inhomogeneous conversion for many modern ultrafast laser systems. Finally, phase-matching bandwidth and other practical considerations are discussed.

2.1 THEORETICAL ANALYSIS

2.1.1 The Second Harmonic Amplification (SHA) Wave-Mixing System

We use the naming convention of 'idler' to mean the unseeded wave in OPA. Incorporating idler SHG with OPA results in coupled evolution equations for four nondegenerate fields,

$$d_z A_s = i\frac{\omega_s d_{\text{eff}}}{\mathrm{n}_s c} A_p A_i^* e^{i\Delta k_{OPA} z} \tag{2.1a}$$

$$d_z A_p = i\frac{\omega_p d_{\text{eff}}}{\mathrm{n}_p c} A_s A_i e^{-i\Delta k_{OPA} z} \tag{2.1b}$$

$$d_z A_i = i\frac{\omega_i d_{\text{eff}}}{\mathrm{n}_i c}\left[A_p A_s^* e^{i\Delta k_{OPA} z} + A_{2i} A_i^* e^{i\Delta k_{SHG} z}\right] \tag{2.1c}$$

$$d_z A_{2i} = i\frac{\omega_{2i} d_{\text{eff}}}{2\mathrm{n}_{2i} c} A_i^2 e^{-i\Delta k_{SHG} z}, \tag{2.1d}$$

where A_j, ω_j, and n_j for $j \in \{s, p, i, 2i\}$ are the signal, pump, idler, and idler second harmonic (SH) electric field amplitudes, angular frequencies, and indices of refraction, respectively. The nonlinear coefficient, d_{eff}, is proportional to the tensor element of the quadratic susceptibility for the specific field polarizations of the involved waves. For simplicity, we have assumed collinear waves where all frequencies are far below electronic resonances (i.e., negligible loss), and thus Kleinman symmetry implies d_{eff} is identical for the OPA and SHG processes [46]. The OPA wave-vector mismatch is given by $\Delta k_{OPA} = k_p - k_s - k_i$ and the SHG wave-vector mismatch is given by $\Delta k_{SHG} = k_{2i} - 2k_i$, where $k_j = \omega_j \mathrm{n}_j / c$. The above system was first studied under the condition of perfect phase matching in the context of self-doubling optical parametric oscillation (OPO) [3, 42].

When $|\Delta k_{SHG}| \gg 0$, the SHG process cannot deplete energy from the OPA sys-

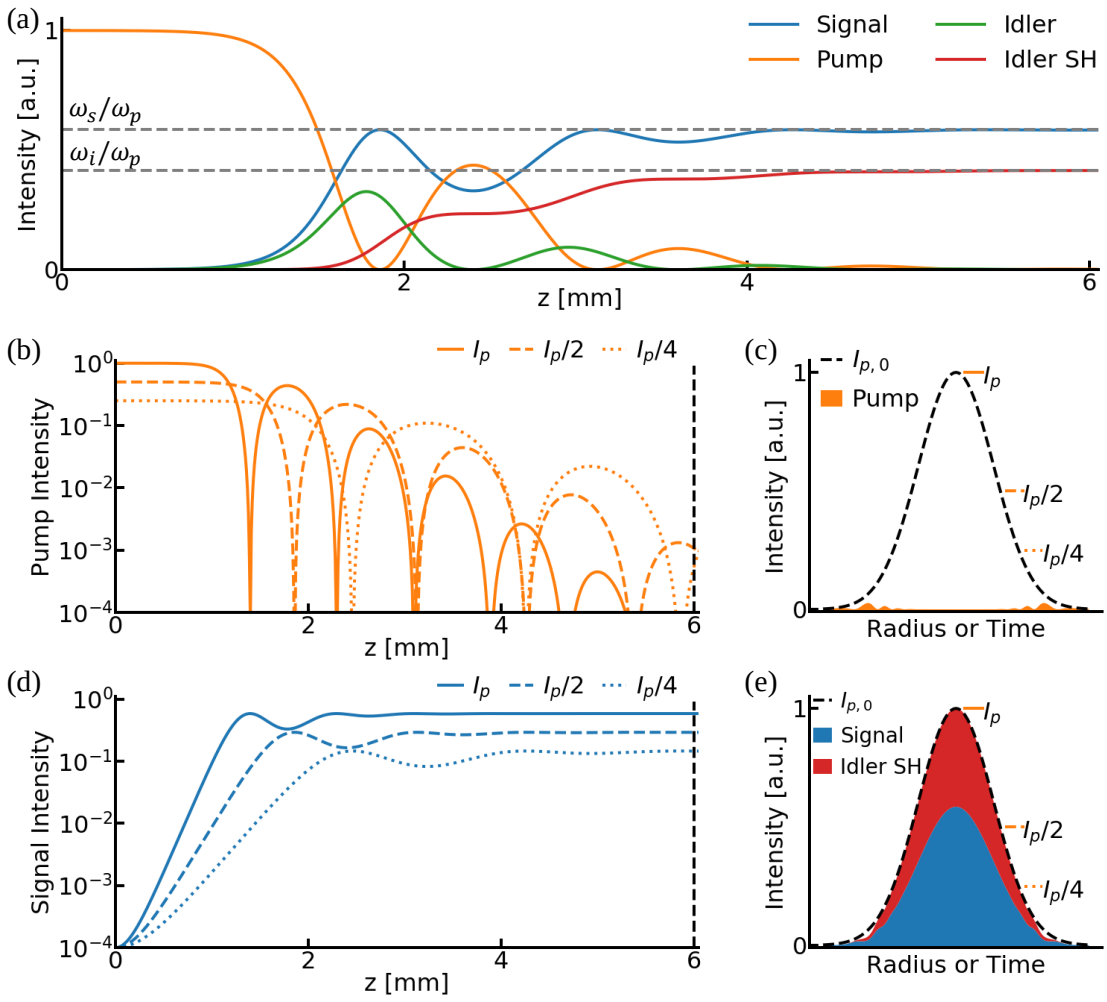

Figure 2.2: (a) Evolution dynamics of SHA. The idler is converted to its SH during OPA gain saturation, damping signal back-conversion and eventually converting all pump energy to signal and idler SH fields, with the evolution dynamics of a damped oscillator. The quantum defect, ω_s/ω_p (dashed line), sets a conversion efficiency upper limit. (b, d) The existence of conversion cycle damping regardless of local pump intensity enables (c, e) spatiotemporally uniform pump depletion at a suitable length (dashed line in (b, d)).

tem significantly and the system dynamics are quantitatively similar to those of ordinary OPA (Fig. 1.1a), with cyclical conversion. However, numerical integration of the four coupled equations when $\Delta k_{SHG} \cong 0$ results in qualitatively different monochromatic, plane-wave evolution dynamics involving the mixing of all four waves (Fig. 2.2a). We may reason that the initial behavior, i.e.,

before the onset of signal gain saturation takes place, is well approximated as pure OPA. This can be seen through examination of the idler evolution equation, Eq. (2.1c). For the case of $\Delta k_{OPA} = \Delta k_{SHG} = 0$, the change to the idler wave is equally weighted by a gain term, $A_p A_s^*$, and a loss term, $A_{2i} A_i^*$. However, for the initial conditions of an optical parametric amplifier, $|A_{p,0}| \gg |A_{s,0}|$ and $A_{i,0} = A_{2i,0} = 0$, gain must strongly exceed loss until significant pump depletion occurs and thus $|A_p| \approx |A_s| \approx |A_i|$. These initial dynamics are illustrated in Fig. 2.2a, with little observed deviation from ordinary OPA evolution through the first conversion peak.

Significant idler SH intensity appears shortly before full pump depletion, at which point qualitative changes to the behavior compared to conventional OPA are observed in the form of damped oscillations of energy between the pump, signal and idler, with a step-wise monotonic displacement of intensity to the idler SH. We refer to this hybrid process as SHA. The pump and idler fields reduce asymptotically to zero intensity while the signal field asymptotically approaches its quantum-defect-limited intensity (i.e., the creation of one signal photon for each annihilated pump photon). The SH intensity asymptotically approaches $(\omega_{2i}/2\omega_p) = (\omega_i/\omega_p)$ times the initial pump intensity (i.e., the creation of one idler SH photon for every two annihilated pump photons). A reversal of the process is not observed. We note that similar behavior was observed in self-doubling OPO when investigated numerically in single-pass operation, where in contrast the investigation studied the case of the signal (seeded wave), rather than the idler, experiencing simultaneous SHG [3].

A number of experimental works have observed signal or idler SHG simultaneously phase matched during OPA (often as an undesired, parasitic process,

though sometimes with the goal of obtaining the upconverted wave, see, e.g., [84] for some examples), but without investigating the four-wave dynamics occurring beyond the first conversion peak. Here we observe that the dynamics of SHA beyond the first conversion half-cycle enable a solution to the spatiotemoporal inhomogeneous conversion problem of OPA. Independence of the qualitative dynamics to the local initial pump intensity can be seen in Fig. 2.2b; at lower intensity, the dynamics are merely slowed. As in QPA, efficiency optimization can now be carried out in a different way from the conventional approach. Rather than choosing a crystal length where the greatest fraction of the spatiotemporal energy distribution is close to the first conversion peak, a crystal length is chosen at which the conversion oscillations have been damped over the majority of the spatiotemporal extent (Fig. 2.2c), thus allowing nearly full pump depletion and conversion.

2.1.2 Damped Duffing Oscillator Universal Model of Parametric Amplification

Further insight into the nonlinear evolution dynamics can be gained by nondimensionalizing Eqs. (2.1):

$$d_\zeta u_p = i u_s u_i e^{-i\Delta_{OPA}\zeta} \tag{2.2a}$$

$$d_\zeta u_s = i u_p u_i^* e^{i\Delta_{OPA}\zeta} \tag{2.2b}$$

$$d_\zeta u_i = i u_p u_s^* e^{i\Delta_{OPA}\zeta} + i2\gamma_0 u_{2i} u_i^* e^{i\Delta_{SHG}\zeta} \tag{2.2c}$$

$$d_\zeta u_{2i} = i\gamma_0 u_i^2 e^{-i\Delta_{SHG}\zeta}. \tag{2.2d}$$

The $u_j = \sqrt{2n_j\epsilon_0 c/\hbar\omega_j F_0}A_j$ are nondimensional electric field amplitudes for $j \in \{p, s, i, 2i\}$, $\zeta = \Gamma_{OPA} z$ is a nondimensionalized propagation coordinate, and

$\Delta = \Delta k/\Gamma_{OPA}$ is a nondimensional wave-vector mismatch. $F_0 = \sum_j 2\mathrm{n}_j\epsilon_0 c\,|A_j(z=0)|^2/\hbar\omega_j$ is the total initial photon flux, e.g., $F_0 = 2n_p\epsilon_0 c\left|A_p(z=0)\right|^2/\hbar\omega_p + 2n_s\epsilon_0 c\,|A_s(z=0)|^2/\hbar\omega_s$ for conventional OPA where only the pump and signal fields are seeded. Apart from the wave-vector mismatches, the single remaining system parameter, $\gamma_0 = \Gamma_{SHG}/2\Gamma_{OPA}$, is a ratio of SHG and OPA drive strengths, where $\Gamma_{OPA} = \sqrt{\hbar\omega_p\omega_s\omega_i d_{\mathrm{eff}}^2 F_0/2\mathrm{n}_p\mathrm{n}_s\mathrm{n}_i\epsilon_0 c^3}$, and $\Gamma_{SHG} = \sqrt{\hbar\omega_i^2\omega_{2i} d_{\mathrm{eff}}^2 F_0/2\mathrm{n}_i^2\mathrm{n}_{2i}\epsilon_0 c^3}$. This parameter is purely a function of material refractive indices and wave frequencies: $\gamma_0 = \sqrt{\mathrm{n}_p\mathrm{n}_s\omega_i\omega_{2i}/4\mathrm{n}_i\mathrm{n}_{2i}\omega_p\omega_s}$.

The fraction of photons in the jth field relative to the total number of initial photons, which we refer to as the fractional photon number of the jth field, is given by $n_j \equiv \left|u_j\right|^2$. There are two independent Manley-Rowe equations describing conservation of fractional photon number,

$$1 = n_p(\zeta) + n_s(\zeta) \tag{2.3a}$$

$$n_{p,0} = n_p(\zeta) + n_i(\zeta) + n_d(\zeta), \tag{2.3b}$$

where $n_d(\zeta) = 2n_{2i}(\zeta)$ is the fraction of idler photons displaced to the idler SH field. In addition to the total initial photon flux, F_0, another initial condition that must be specified for OPA is the ratio of initial pump and signal photon number. From the first Manley-Rowe equation it can be seen that only one of $n_{p,0} \equiv n_p(0)$ or $n_{s,0} \equiv n_s(0)$ is necessary to specify this initial condition. It should be noted that the quantity $n_{s,0}^{-1} = (n_{p,0}+n_{s,0})/n_{s,0}$ is equal to the maximum possible signal photon gain, which is obtained when each pump photon at the start of the process is converted to a signal photon. Fig. 2.3(a) illustrates the four-wave SHA dynamics in terms of fractional photon numbers for $\gamma_0 = 0.35$ and initial condition $n_{s,0} = 0.1$.

Additional insight into the dynamics can be obtained by examining a single-

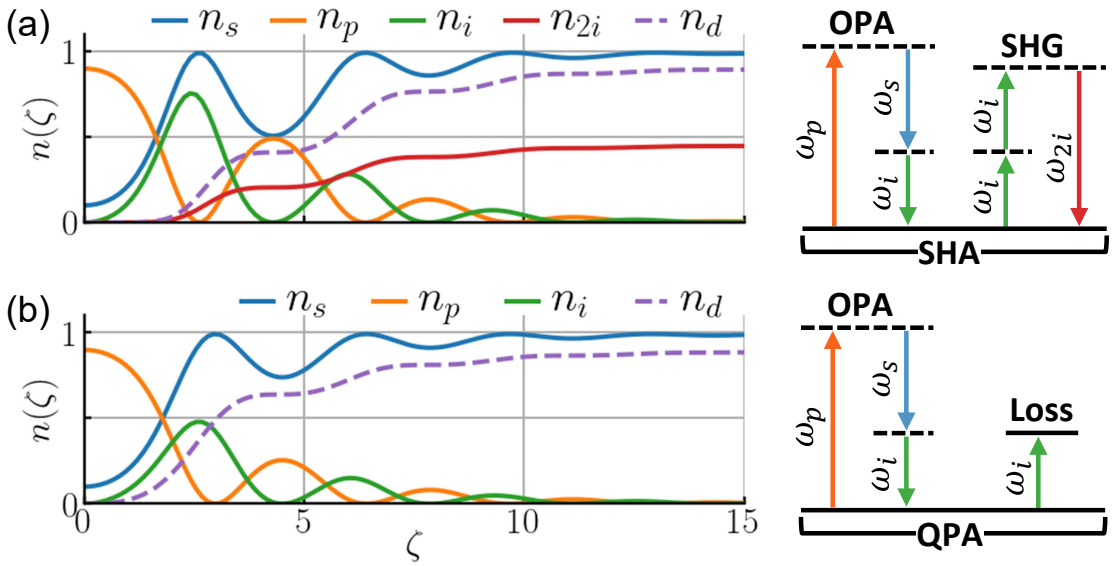

Figure 2.3: Fractional photon number exchange dynamics under perfect phase matching conditions and corresponding photon mixing diagrams for OPA processes involving the displacement of idler photons. (a) SHA: OPA with simultaneous idler SHG. (b) QPA: OPA with simultaneous idler linear absorption. All cases: $\gamma_0 = 0.35$, $n_{p,0} = 0.9$. n_d is fractional photon number of displaced idler photons.

field equation for the pump obtained from Eqs. (2.2) by use of the Manley-Rowe equations. Setting $\Delta_{OPA} = \Delta_{SHG} = 0$, we differentiate Eq. (2.2a) and combine with Eqs. (2.2b), (2.2c), (2.3a) and (2.3b) to find:

$$d_\zeta^2 u_p = -\left(1 + n_{p,0} - n_d(\zeta)\right) u_p + 2u_p^3 - 2\gamma(\zeta) d_\zeta u_p, \tag{2.4}$$

where we have assumed OPA initial conditions and that $u_{p,0}$ and $u_{s,0}$ are positive real, from which it follows that $u_i = -u_i^*$ and $u_{2i} = -i\,|u_{2i}|$.

Equation (2.4) for the pump field is the force equation of a damped, undriven Duffing oscillator. The first term is a linear restoring force that decreases as the number of displaced idler photons, $n_d(\zeta) = 2n_{2i}(\zeta)$, grows. The second term acts as a nonlinear softening of the restoring force. Under the constraints of OPA initial conditions and the Manley-Rowe equations, the sum of the first two terms must always be negative (i.e., the force is always restoring). The third term re-

sults in damping given by the coefficient $\gamma(\zeta) = \gamma_0 \sqrt{n_d(\zeta)/2} = \gamma_0 \sqrt{n_{2i}(\zeta)} = \gamma_0 u_{2i}$, which grows monotonically from zero as idler photons are unidirectionally displaced to the idler SH field. While u_i may switch signs between conversion cycles, u_{2i} does not since it grows in proportion to u_i^2 (Eq. (2.2d), with $\Delta_{SHG} = 0$). Thus, $\gamma(\zeta)$ never switches sign, meaning the oscillator is always damped and never experiences gain.

We note, when $\gamma(\zeta) = 0$ (i.e., when there is no SHG), Eq. (2.4) corresponds to the case of conventional OPA, and is the undamped, undriven cubic Duffing equation, $d_\zeta^2 u_p = -(1 + n_{p,0})u_p + 2u_p^3$, which is well known to have Jacobi elliptic function solutions [80], the known solutions to OPA [2].

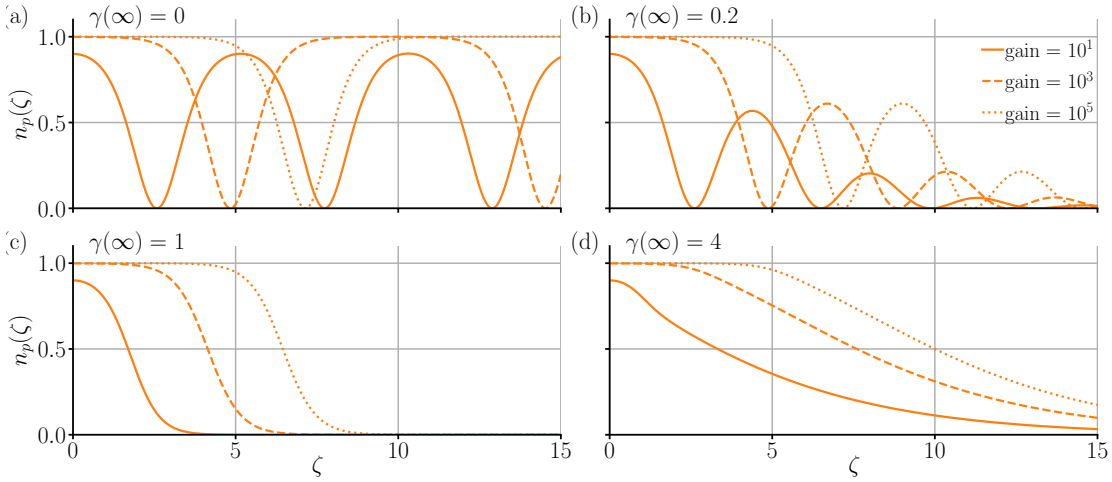

Figure 2.4: Pump fractional photon number evolution obtained by numerical solution of Eqs. 2.2 under various damping conditions, $\gamma(\infty) = \gamma_0 \sqrt{n_{p,0}/2}$, and initial fractional signal photon number, $n_{s,0}$. These can be understood in terms of the Duffing equation model as the damping regimes of an anharmonic oscillator: (a) undamped: $\gamma(\infty) = 0$ (no SHG), (b) underdamped: $\gamma(\infty) = 0.2$ (stronger OPA), (c) critically damped: $\gamma(\infty) = 1$ (stronger SHG), and (d) overdamped: $\gamma(\infty) = 4$ (much stronger SHG). $n_{s,0} = 0.1$, 0.001, and 0.00001 correspond to a maximum signal photon gain of 10 (solid), 30 (dashed), and 50 dB (dotted), respectively.

In terms of the Duffing equation, Eq. (2.4), the system parameter γ_0 can now be understood as a damping parameter. Since the damping coefficient of

the Duffing equation, $\gamma(\zeta)$, is dependent on the number of photons in the idler SH field (an evolving quantity), one might not expect evolution with the standard characteristics of a damped oscillator. However, since the fractional idler SH photon number monotonically approaches a steady-state value, $n_{2i}(\infty) = \lim_{\zeta\to\infty} n_{2i}(\zeta) = n_{p,0}/2$, the damping coefficient also monotonically approaches a steady-state value related to γ_0 by $\gamma(\infty) = \lim_{\zeta\to\infty} \gamma(\zeta) = \gamma_0 \sqrt{n_{2i}(\infty)} = \gamma_0 \sqrt{n_{p,0}/2} \simeq \gamma_0/\sqrt{2}$. Indeed, Fig. 2.4, which shows a numerical solution of Eqs. (2.2) for $\gamma(\infty) = 0$, 0.2, 1.0, and 4.0, clearly depicts the four regimes of a damped oscillator: undamped, underdamped, critically damped, and overdamped, respectively. By virtue of $\gamma_0 = \Gamma_{SHG}/2\Gamma_{OPA}$, and thus $\gamma(\infty) \simeq \gamma_0/\sqrt{2} = \Gamma_{SHG}/2\sqrt{2}\Gamma_{OPA}$, these values of $\gamma(\infty)$ also correspond to no SHG, stronger OPA, stronger SHG, and much stronger SHG, respectively. For each value of $\gamma(\infty)$, the dynamics of $n_p(\zeta)$ are shown for three initial values of $n_{s,0}$ corresponding to 10, 30, and 50 dB photon gain. The effect of a decreased initial fractional signal photon number (higher gain) is primarily a delay of the onset of the oscillatory dynamics. Once they begin, the oscillations have nearly identical amplitude, frequency, and decay rate. Notably, by Eq. (2.3a), in each case the signal fractional photon number asymptotically approaches 1, meaning every pump photon produces a signal photon, equivalent to the full quantum-defect-limited conversion efficiency in energy, $I_s = I_{s,0} + (\omega_s/\omega_p)I_{p,0}$.

For a practical amplifier device, regimes near critical damping (Fig. 2.4c) are ideal from a design perspective as oscillations are avoided and convergence to full pump depletion occurs at the shortest length. We note, when indices of refraction $\mathrm{n}_p \approx \mathrm{n}_s \approx \mathrm{n}_i \approx \mathrm{n}_{2i}$ (as is typical for four off-resonant fields) the damping parameter $\gamma(\infty)$ reduces to $\approx \sqrt{\omega_i\omega_{2i}/2\omega_p\omega_s}$. Thus, critical damping occurs when the signal and idler frequencies are related by the ratio $\omega_i/\omega_s \approx$

$(1 + \sqrt{5})/2$, the golden ratio. We note, in this regime, $\omega_{2i} > \omega_p$, providing a route to efficient upconversion of a laser through generation of the idler SH.

As SHA is a conservative, closed nonlinear system, its close resemblance to a dissipative system is remarkable, and begs comparison of SHA to OPA with actual loss, i.e. QPA, where irreversible removal of idler photons is achieved by linear absorption [60, 61] rather than by SHG. This is modeled by replacement of Eq. (2.2c) with

$$d_\zeta u_i = i u_p u_s^* e^{i\Delta_{OPA}\zeta} - \frac{\alpha}{\Gamma_{OPA}} u_i, \tag{2.5}$$

where the loss coefficient, α, is positive real. Numerical integration of Eqs. (2.2a), (2.2b) and (2.5) (Fig. 2.3b) illustrates QPA evolution dynamics remarkably similar to those of SHA when the coefficient to the linear loss term in Eq. (2.5) (α/Γ_{OPA}) is equivalent to the coefficient to the nonlinear loss term in Eq. (2.2c) ($\Gamma_{SHG}/\Gamma_{OPA}$), or when $\alpha = \Gamma_{SHG}$. Indeed, the QPA system can be cast in the Duffing oscillator form, Eq. (2.4), using $n_d(\zeta) = \frac{2\alpha}{\Gamma_{OPA}} \int_0^\zeta n_i(\zeta) d\zeta'$, which measures the fractional number of photons lost due to linear absorption, and $\gamma(\zeta) = \alpha/2\Gamma_{OPA}$, now a constant (non-evolving) damping parameter. Thus, the Duffing oscillator can serve as a universal model, capturing conventional OPA (an undamped oscillator with nonlinear restoring force), QPA (dissipative OPA with linear idler loss causing oscillation damping), and SHA (a conservative, hybridized parametric system in which oscillation damping is caused by the displacement of idler photons by SHG), with the respective parameters of Eq. (2.4) summarized in Table 2.1.

While QPA and SHA exhibit close dynamical behavior, a key physical distinction is that an incoherent linear loss mechanism prevents coupling of the lost energy back to the system in QPA, while the idler SH field of SHA coherently

Nonlinear Process	$n_d(\zeta)$	$\gamma(\zeta)$
OPA	0	0
SHA	$2n_{2i}(\zeta)$	$\gamma_0\sqrt{n_{2i}(\zeta)}$
QPA	$\frac{2\alpha}{\Gamma_{OPA}}\int_0^\zeta n_i(\zeta)d\zeta'$	$\frac{\alpha}{2\Gamma_{OPA}}$

Table 2.1: Parameters of the Duffing oscillator equation, Eq. (2.4), for each process. $n_d(\zeta)$ is the fractional photon number displaced from the idler field by loss (QPA) or SHG (SHA) and $\gamma(\zeta)$ is a damping parameter.

drives the idler field throughout propagation and the irreversibility of power flow from idler to idler SH is a consequence of the coherent dynamics at degeneracy. This phenomenon enables the conservative SHA system to have a loss-like channel – mimicking a heat bath – through its full nonlinear evolution. These distinctly different physical damping mechanisms have different practical consequences. In QPA, idler photons are dissipated by material absorption and lost as heat, while in SHA, a nonlinear polarizability converts them to a coherent copropagating wave. At the end of the medium, this wave can be separated from the amplified signal by a beamsplitter, allowing complete removal and possible reuse of its energy.

2.2 NUMERICAL ANALYSIS: SPATIOTEMPORAL PROPAGATION

We employed a spatiotemporal propagation analysis for coupled signal, pump, idler, and idler SH waves to predict the success of two realistic amplifier designs based on SHA. Propagation equations for *cw* fields of finite spatial width including diffraction and Poynting vector beam walk-off were first employed to identify a range of beam sizes where these spatial propagation effects play a

negligible role in the field evolution (see *Appendix A*). The four coupled equations for femtosecond pulse propagation were then solved for beam sizes within this range for each spatial coordinate independently, using the exact material dispersion given by Sellmeier equations. This allowed us to perform a full spatiotemporal analysis of all non-negligible propagation effects consistent with a collinear geometry. Nonlinear polarization terms beyond quadratic order were not included. (See *Appendix B* for propagation equations.)

To reflect the bell-shaped profiles of real lasers, in all simulations, the initial pump and signal intensity profiles were 1st-order Gaussian in both temporal and spatial extent. The two spatial beam dimensions were set equal and rotational symmetry about the propagation axis is assumed. The peak intensity of the pump was chosen to be below the reported damage threshold of each nonlinear medium. Pulse durations are given in FWHM and beam radius in $1/e^2$ dimension.

2.2.1 Birefringent Phase Matching in CSP

We begin by investigating SHA achieved via birefringent phase matching, a scheme relevant for high-energy amplification in a bulk medium. Our analysis uses CSP, a material relevant to mid-infrared applications of OPA, and a 2.05-μm pump wavelength relevant to Ho- and Tm-doped solid-state gain media. Our analysis predicts that a high-energy 2-μm picosecond laser can be down-converted to 3.0 μm with less than a factor of two loss in energy, a severalfold efficiency improvement compared to standard OPA.

SHA requires simultaneous phase matching of OPA and idler SHG pro-

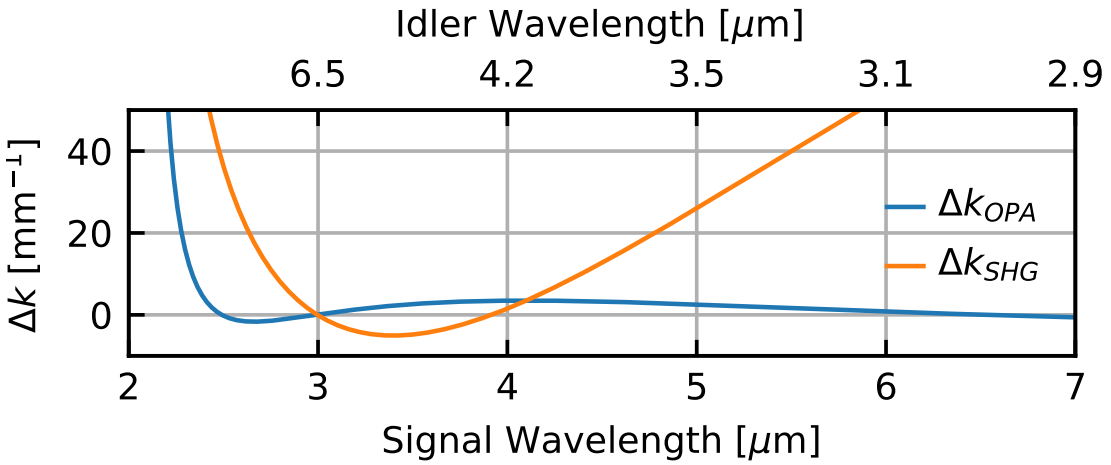

Figure 2.5: Type-I birefringent phase-matching curves for simultaneous OPA (blue) and idler SHG (orange) processes in CSP with tuning angle $\theta = 44.8°$ and a 2.05-μm pump. Simultaneous phase matching occurs for a 3.0-μm signal, corresponding to a 6.5-μm idler and 3.25-μm idler SH. (Sellmeier coefficients taken from [43].)

cesses, or $\Delta k_{OPA} = \Delta k_{SHG} \approx 0$. CSP is uniaxial with broad phase-matching bandwidth for Type-I OPA pumped at 2.05 μm [85, 56]. At a crystal orientation given by $\theta = 44.8°$, simultaneous phase matching occurs at a 3.0-μm signal, corresponding to a 6.5-μm idler and 3.25-μm idler SH (Fig. 2.5). While Δk_{SHG} varies more rapidly with frequency than Δk_{OPA}, our analysis predicts sufficient bandwidth to support efficient SHA for pulses down to ~1 ps.

Fig. 2.6 compares SHA (left column) with standard OPA (right column) for high-gain (50-dB) amplification of a 1-ps, 2-nJ, 2-mm radius, 3.0-μm signal wave in a few millimeters of CSP, pumped by an 870-μJ, 2.05-µm wavelength pump of the same duration and 1-mm radius, corresponding to a peak intensity (50 GW/cm^2) below the damage threshold of CSP. These parameters correspond to $\gamma_0 = 0.27$, putting the SHA system in the underdamped regime. In SHA (Fig. 2.6a,e), the evolution of energy exchange over the full spatiotemporal profile of the waves displays an asymptotic approach to full conversion, with

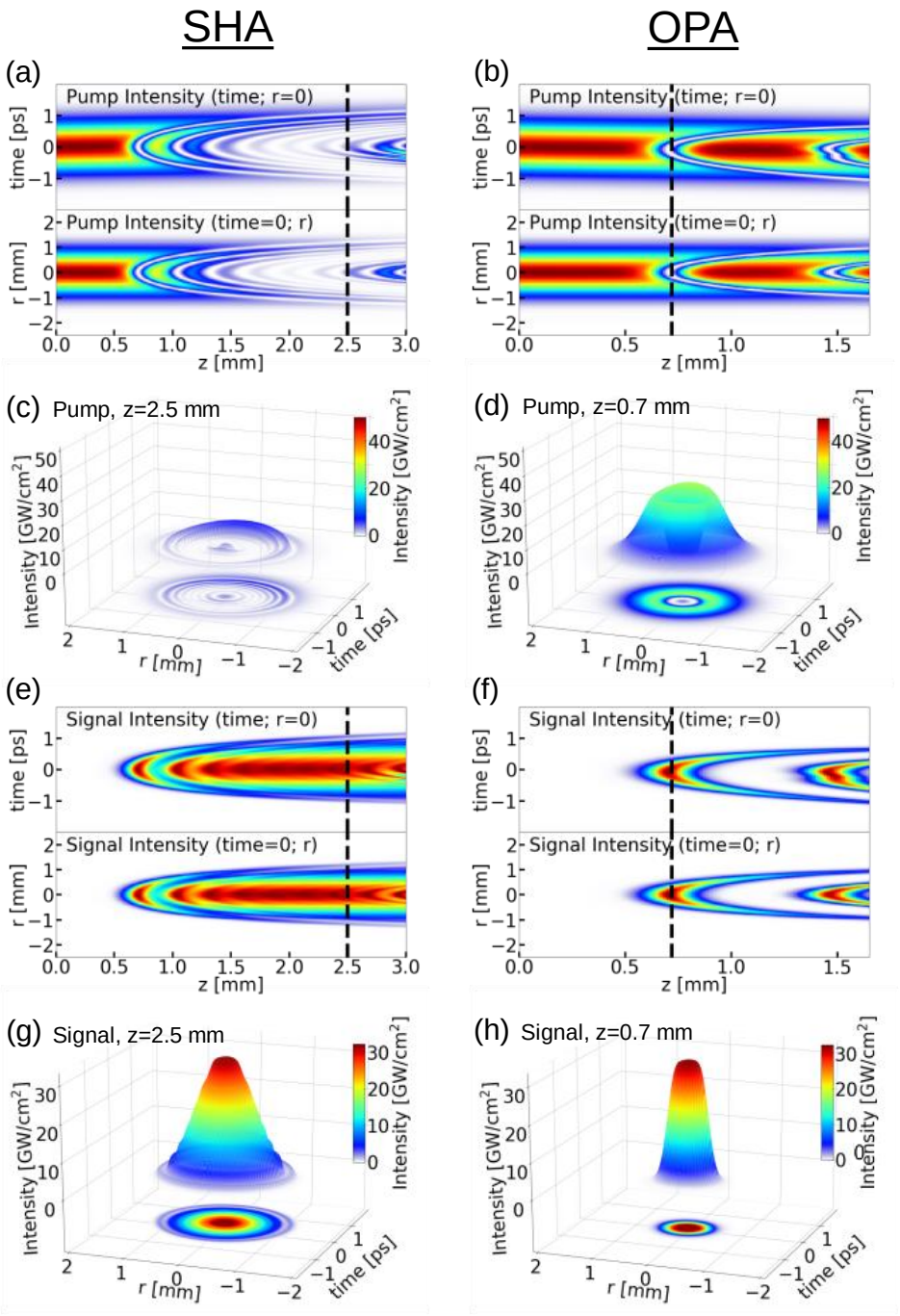

Figure 2.6: Spatiotemporal evolution of SHA (left) vs. conventional OPA (right) in CSP with birefringent phase matching. (a,b) Pump depletion dynamics, with optimum length for conversion efficiency indicated (dashed line). (c,d) Intensity profile of the residual pump at the optimum length. (e,f) Signal amplification dynamics. (g,h) Signal intensity profile at the optimum length. SHA results in 55% pump-to-signal energy conversion vs. 8% for conventional OPA.

damped conversion cycles as typified by underdamping. Full damping at the spatiotemporal profile center for over 1 mm of propagation allows depletion of the spatiotemporal wings to catch up before any significant back-conversion occurs at the center. Back-conversion remains suppressed just past the optimal length of 2.5 mm, where 80% pump depletion (Fig. 2.6c) and 55% energy conversion to the signal (Fig. 2.6g) is observed with $> 10^5$ gain in a single stage. The remaining 45% of the energy is split between the idler at 6.5 μm (3%), the idler SH at 3.2 μm (22%), and the unconverted pump (20%). The effect of temporal walk-off, resulting in a slight temporal asymmetry, is observed but does not significantly interfere with device performance. Fig. 2.7 shows the SHA seed, amplified signal, and idler SH spectra and temporal profiles. The amplified signal takes on the initial pump profile with 1.0-ps duration, i.e., almost no temporal gain narrowing is observed – a result of the near-uniform spatiotemporal conversion. In contrast, for conventional OPA (Fig. 2.6b,d,f,h), only 12% pump depletion and 8% energy conversion to the signal can be achieved (at the optimal length of 0.7 mm, corresponding to approximately one half-period of the conversion-back-conversion cycle at the spatiotemporal peak). Accordingly, significant spatiotemporal gain narrowing of the amplified conventional OPA signal is observed. The conversion efficiency of SHA is ~ 7 times greater than that of conventional OPA in this example.

In Fig. 2.6a,e, we observe an eventual reversal of energy flow in SHA that returns energy to the pump field. Since pulsed laser beams possess a distribution of wave-vectors and frequencies, some phase mismatch is inherent in any real application. Fig. 2.8 shows the intensity dynamics at the center of each pulse ($(x, t) = (0, 0)$). At $z \gtrsim 2$ mm, energy can be observed returning from idler SH to idler field and, subsequently, from signal and idler to pump field. These modi-

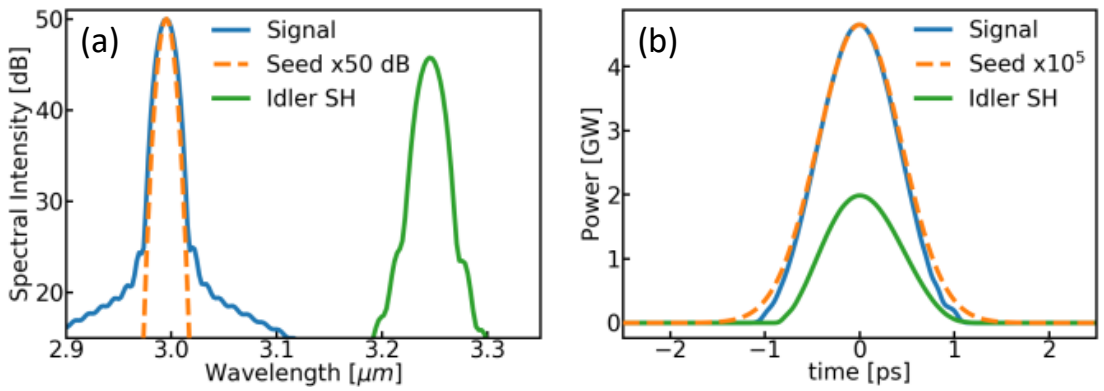

Figure 2.7: Spatially integrated (a) spectra and (b) pulse profiles of amplified signal and idler SH in the CSP SHA device.

fied dynamics are almost exactly matched by numerical integration of Eqs. (2.2) setting either Δk_{SHG} or Δk_{OPA} equal to ± 0.033 mm^{-1} (dotted curves), indicating a nonzero average wave-vector mismatch magnitude.

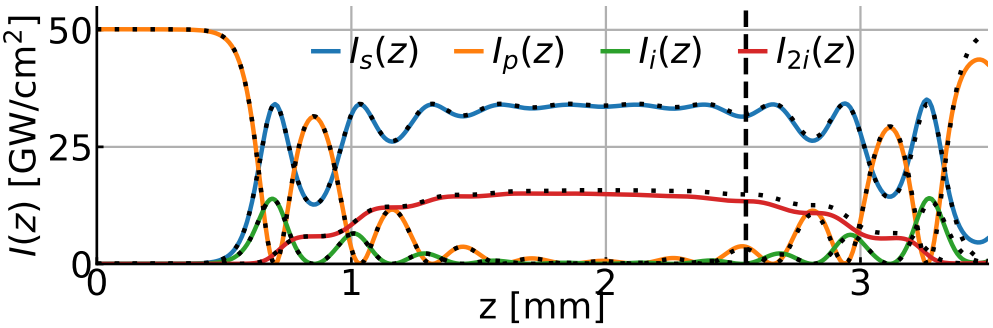

Figure 2.8: Intensity evolution of the four fields at $t = x = 0$ showing eventual back-conversion. Dotted lines: corresponding solution of Eqs. (2.2) for $(\Delta k_{SHG})\Delta k_{OPA} = (-)0.033$ mm^{-1}.

2.2.2 Superlattice Quasi-Phase Matching in LNB

While the introduction of a noncollinear geometry could be used to tune the signal frequency of the birefringent phase matching approach above, QPM offers additional flexibility as well as Type-0 geometries with large nonlinear coeffi-

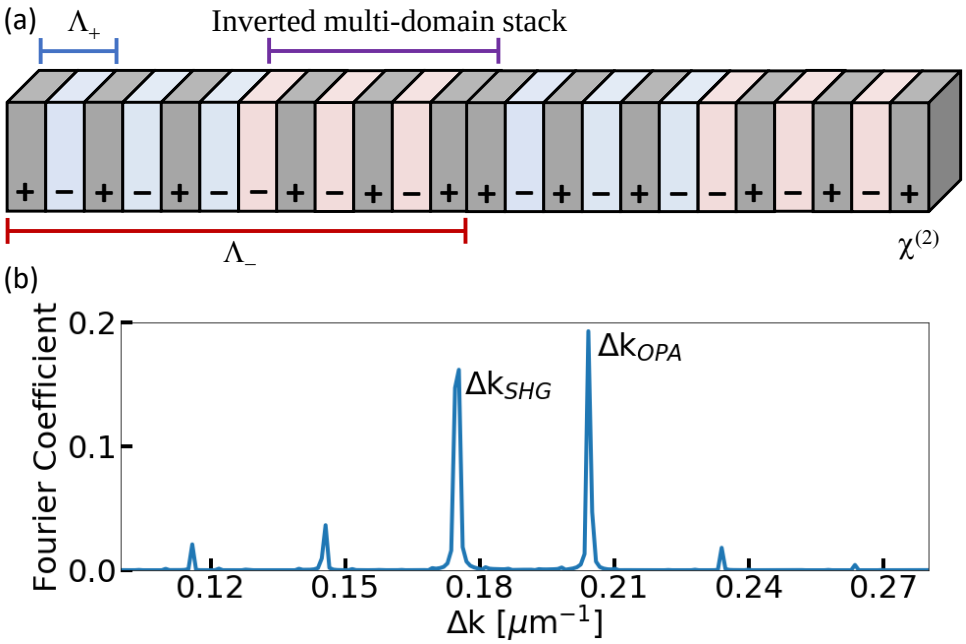

Figure 2.9: (a) Superlattice QPM device schematic. (b) The Fourier transform of a LNB device consisting uniformly of 16.6-μm domains reveals sharp Bragg peaks at Δk_{OPA} and Δk_{SHG}.

cient and the absence of spatial walk-off. In this example, our analysis predicts that a 1-µm pump laser can amplify chirped 180-fs transform-limited (TL) pulses at 1.63 μm in OPCPA configuration in a LNB superlattice QPM device, producing millijoule output with > 50 dB gain and an energy conversion efficiency of 44% – a five-fold efficiency increase compared to standard OPA – while simultaneously producing a chirped 100-fs TL idler SH pulse at 1.40-μm with 21% conversion efficiency.

In a previous study, an aperiodically poled LNB device for simultaneous QPM of OPO and SHG was designed for the purpose of self-doubling OPO [42] using a numerical, iterative approach. Numerous other approaches exist for the design of multiple-process QPM, e.g., [16, 58, 73, 79, 84]. Here we employ the approach of [16], which for the phase matching of two simultaneous processes can have the simple form of a superlattice with inverted 50%-duty-cycle

multi-domain stacks (Fig. 2.9a), where $\Lambda_{\pm} = 4\pi/(\Delta k_{OPA} \pm \Delta k_{SHG})$. We further use a rounding approach: each domain wall of the $\max(\Lambda_+, \Lambda_-)$ periodic lattice is rounded to the nearest domain wall of the $\min(\Lambda_+, \Lambda_-)$ periodic lattice. This final step ensures a QPM structure that only has one manufacturable domain size of width $\min(\Lambda_+, \Lambda_-)/2$ even for noncommensurate values of $\Lambda_{\pm}$, where there are occasionally repeated positive or negative domains.

We designed a superlattice QPM device for SHA with a 1.03 μm pump and 1.63 μm signal in Mg:$LiNbO_3$ in Type-0 configuration (*eee*). Simultaneous SHG doubles the 2.8 μm idler to a 1.4 μm idler SH. The device is generated from superimposed noncommensurate poling periods $\Lambda_+ = 33.2$ μm and $\Lambda_- = 425$ μm with rounding as described above to eliminate small domains, resulting in a structure consisting uniformly of 16.6-μm domains of alternating sign of d_{eff} and some repeated positive or negative domains. The spatial Fourier transform of its domain poling function (Fig. 2.9b) has sharp Bragg peaks with nearly equal magnitude at the exact values of $\Delta k_{OPA} = 0.204/\mu$m and $\Delta k_{SHG} = 0.174/\mu$m.

Numerical integration of the SHA wave-mixing dynamics in this structure illustrates efficient amplification of femtosecond signal pulses (Fig. 2.10). We modeled 50-dB amplification in an OPCPA configuration with a 5.5-ps, 2.7-mJ, 30-GW/cm^2 pump and a 120-fs, 8-nJ, 31-nm FWHM seed at 1.63 μm chirped to 5.6 ps. These chirped pulse durations mitigated the effects of group-velocity walk-off. Fig. 2.10a,c shows clear underdamped SHA dynamics. At 7.4 mm, nearly homogeneous depletion of the pump in space and time is observed (Fig. 2.10b), resulting in 68% pump energy depletion with 44% going to the signal (1.2 mJ, Fig. 2.10d) with a 180-fs FWHM TL pulse duration and 21% going to a 1.40-μm, 100-fs TL idler SH (Fig. 2.10e,f). For comparison, a standard periodically

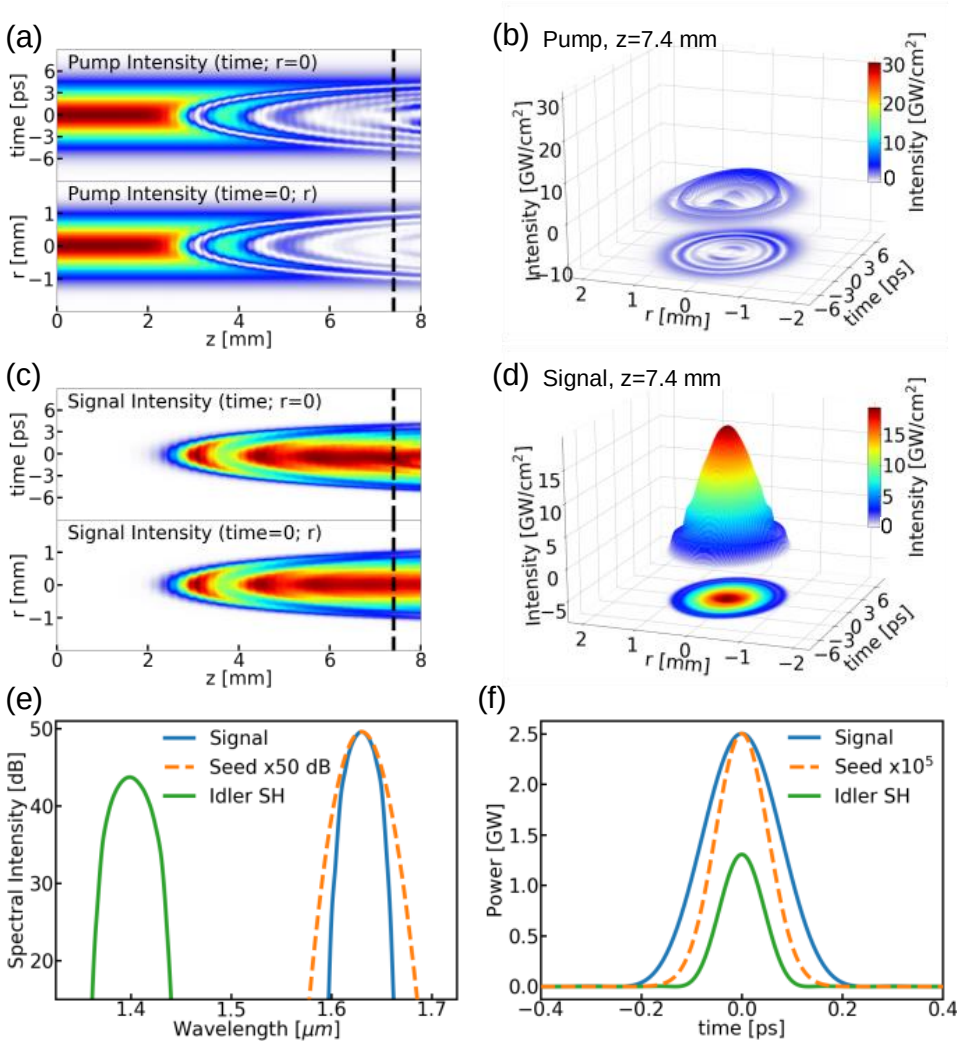

Figure 2.10: Spatiotemporal evolution of a LNB superlattice QPM device employing SHA to efficiently amplify femtosecond near-IR pulses in OPCPA configuration. (a,c) Pump and signal dynamics, indicating spatiotemporally homogeneous amplification at a length of 7.4 mm, resulting in 44% pump-to-signal energy conversion. (b,d) Pump and signal profiles at 7.4 mm. (e) Spectra indicating 50-dB signal amplification. (f) TL pulse durations of 180 fs and 100 fs for amplified signal and idler SH, respectively.

poled QPM structure optimized for conventional OPA (not shown) results in 15% pump energy depletion, with only 9% of the pump energy going to the signal – a 5-fold decrease.

2.3 DISCUSSION

A detailed study of the phase matching of SHA in common OPA materials is beyond the scope of this article, but here we discuss several important considerations. In the example of birefringent phase matching above (Section 2.2.1), we observed efficient amplification of a 1-ps pulse. This example was chosen to make use of the full phase-matching bandwidth available for the chosen pump and signal wavelengths in a collinear geometry. The phase-matching constraints for simultaneous OPA and SHG are naturally greater than those of either process alone; as was the case in this example (Fig. 2.5), the two processes have greatly different gradients $d\Delta k/d\lambda_s$, and the larger gradient sets the bandwidth of the joint process. Thus, e.g., even if the OPA phase-matching bandwidth is broad, a narrow SHG phase-matching bandwidth can lead to a narrow SHA bandwidth. In the example of QPM in LNB (Section 2.2.2), both $d\Delta k_{OPA}/d\lambda_s$ and $d\Delta k_{SHG}/d\lambda_s$ were small enough at the crossing point of the phase-matching curves to allow for efficient amplification of sub-200 fs pulses.

Specification of the phase-matching bandwidth for SHA in terms of system parameters is less straightforward than for OPA. As seen in Fig. 2.8 (dotted lines), a nonzero wave-vector mismatch in either the OPA or SHG process causes an eventual reversal of the conversion dynamics, with conversion-back-conversion oscillations growing until the system returns a significant portion of

the energy to the pump. For efficient conversion in SHA, the goal is for every frequency to experience fully damped pump-signal conversion cycles. Thus, an essential question is whether a return of power to the pump wave due to wave-vector mismatch sets in before the conversion cycles are fully damped. Fig. 2.11a,b shows the dependence of the length at which a reversal of the dynamics occur on Δk_{OPA} and Δk_{SHG}, respectively. In either case, if Δk is small enough, a window in z-space exists where conversion cycles are fully damped, allowing efficient SHA. For the particular case shown in Fig. 2.11, $|\Delta k| = 1.0\ \mathrm{mm}^{-1}$ appears to be the marginal value. Thus, one would expect that as long as all involved frequencies possess $\Delta k_{OPA}, \Delta k_{SHG} < 1.0\ \mathrm{mm}^{-1}$, a length exists at which all frequencies experience fully damped SHA, and mostly uniform spatiotemporal pump depletion can still take place.

However, notably, the quantitative effects of small nonzero $|\Delta k_{SHG}|$ and $|\Delta k_{OPA}|$ are nearly identical, and Fig. 2.11c shows that one may even be used to partially offset the other. The dynamical behavior associated with nonzero Δk_{SHG} is intuitive: $\Delta k_{SHG} z = \pi$ reverses the displacement of idler photons to the idler SH, turning idler loss into idler gain in Eq. (2.1c) and thus causing oscillations to grow rather than to decay. The similar effect on the dynamics due to nonzero Δk_{OPA}, however, is less intuitive, and requires additional study. We note that the offsetting behavior of two wave-vector mismatches common to a single field has been noted earlier in the context of cascaded third-order processes [22]. Further investigation of the offsetting behavior in SHA also requires further study.

Collinear birefringent phase matching of idler SHG requires a specific material orientation, e.g., the theta angle for a uniaxial crystal, and so choice of

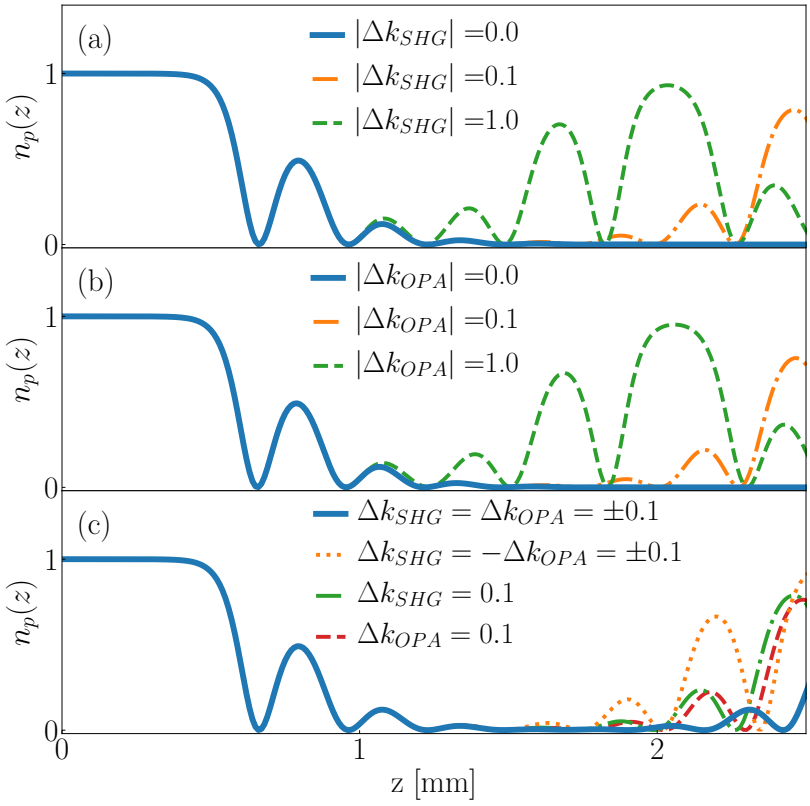

Figure 2.11: Effects of small wave-vector mismatch (in mm^{-1}) on SHA for $\gamma_0 = 0.35$ and $\Gamma_{OPA} = 13\ \text{mm}^{-1}$. (a) Nonzero Δk_{SHG} leads to the eventual return of conversion-back-conversion cycles and regrowth of the pump wave. (b) A nearly identical effect is seen for nonzero Δk_{OPA}. (c) Simultaneous wave-vector mismatch of the two processes can enhance or partially offset the regrowth of the pump, depending on the relative signs of Δk.

an idler wavelength fixes the theta angle. Once this is fixed, there is only one free parameter available for phase matching the OPA process: the pump wavelength or signal wavelength, since they are related by the OPA requirement $\omega_p - \omega_s = \omega_i$. As a result, for any pump wavelength and given nonlinear medium, in a collinear geometry there is likely only one signal wavelength (and corresponding idler) where $\Delta k_{SHG} = \Delta k_{OPA} = 0$. However, the use of a non-collinear angle between pump and signal should enable signal-wavelength tunable SHA for a given pump wavelength through the additional degree of

freedom for phase matching. A superlattice QPM structure with Bragg peaks at both Δk_{SHG} and Δk_{OPA}, as used in Section 2.2.2, can also provide arbitrary choice of signal and pump wavelengths within a range. Thus, in practice, non-collinear birefringent phase-matching and QPM allow some flexibility of choice of the signal wavelength that is required for a particular application. Alternatively, if the shortest possible duration is desired, one might select the signal wavelength that has the broadest phase-matching bandwidth. This approach allowed us to obtain a TL bandwidth supporting a sub-200-fs pulse by QPM in Section 2.2.2. It is unclear whether the phase-matching of SHA for few-cycle pulse applications will be feasible. However, the joint use of QPM and noncollinear angle is one possible avenue for investigation.

With phase-matching bandwidths supporting amplification of pulses down to sub-ps duration, SHA is clearly relevant to the down-conversion of many high-energy and high-average-power solid-state lasers. In the investigated CSP device, for example, a picosecond 2-μm laser is converted to a 3-μm amplified signal with >50% energy efficiency. SHA therefore provides a route to efficiently translate the frequency of picosecond solid-state lasers. As it works in ordinary bulk nonlinear media without absorption, SHA appears particularly well suited for high energy and high average power applications. As noted earlier, SHA can also up-convert the pump wave to a fractional harmonic of the pump frequency, producing an idler SH with frequency $1 < \omega_{2i}/\omega_p < 2$, when $\omega_i > \omega_s$. SHA is therefore also relevant to the up-conversion of ultrafast solid state lasers, which, if a frequency other than $2\omega_p$ is desired, normally requires an inefficient two-stage device consisting of sequential OPA and SHG (in either order). Thus, SHA can be expected to allow a significantly improved up-conversion efficiency.

For high efficiency, we note it is essential to seed the amplifier only with wavelengths that are appropriately phase-matched for *both* OPA and SHG processes. For example, if part of the seeded bandwidth is phase-matched for OPA only, this component of the pulse will compete for gain and experience ordinary OPA dynamics that lead to spatiotemporally inhomogeneous and inefficient amplification. Furthermore, to enable full depletion of the pump wave, its entire spatiotemporal extent should be overlapped with adequate seed field. For this reason, seed intensity profile sizes should be equal to or larger than the co-propagating pump profiles, as was the case in each of the device investigations of Section 2.2.

We note that for devices operating in the underdamped regime, a consequence of a finite propagation length is that the signal's spatiotemporal profile will exhibit a small modulation that grows in amplitude toward the edge of the profile, as observed in Figs. 2.6 and 2.10. This modulation period is roughly 2-5 times the $1/e^2$ radius of the beam for the two devices studied here and will lead to the higher spatial frequency content of the signal beam diffracting away at roughly 4-25 times the rate of diffraction for the main Gaussian beam in the absence of relay imaging.

In summary, we have found the evolution dynamics of hybridized OPA and idler SHG – a process we have termed 'second harmonic amplification' – to be suited to overcome one of the major problems limiting the conversion efficiency of parametric amplifiers: the spatiotemporally inhomogeneous conversion that is a result of the intensity-dependent conversion-back-conversion cycles that typify the evolution dynamics of conventional OPA. The dynamics of SHA are those of a damped anharmonic oscillator, describable by a Duffing oscillator

model that also describes the dynamics of conventional OPA and OPA with linear idler loss (as due to absorption). Our analysis thus unifies the description of OPA and its variants that incorporate the displacement of idler photons – including the recently demonstrated QPA approach [60, 61] – and may be useful for the analysis and design of many parametric amplifier systems.

Moreover, two device examples provided and investigated by a numerical analysis indicate a high expected pump-to-signal energy conversion efficiency (as high as 55% in one example) in common bulk nonlinear media used for OPA and for the bell-shaped pump beam and pulse profiles commonly obtained from pump lasers. Our examples included devices pumped by picosecond lasers at 1-μm and 2-μm wavelength that produce amplified signal pulses and accompanying idler SH pulses with picosecond and < 200-fs TL duration. SHA is thus predicted to be a concept for back-conversion suppression and high efficiency in OPA with relevance to many applications, and may be especially useful for extending the reach and lowering the cost of high-power OPA-based laser systems. SHA might also be used for efficient upconversion of a pump laser to a selectable fractional harmonic frequency. Further exploration of the birefringent phase-matching range of common materials for SHA, including noncollinear geometry and temperature tuning approaches, and multi-process QPM techniques as well, may lead to wide applicability. An initial analysis of amplifier bandwidth and the dynamics of phase-mismatched SHA was given, but a more expansive analysis – including an investigation of bandwidths approaching the few-cycle limit – will be important for the possible expansion of the SHA approach to the few-cycle regime.

[1]

[1]This chapter is derived from [31] with small changes.

CHAPTER 3

EXPERIMENTAL DEMONSTRATION OF OPTICAL PARAMETRIC AMPLIFICATION EFFICIENCY ENHANCED BY SIMULTANEOUS SECOND HARMONIC GENERATION

Here we present a first experimental demonstration of a new fully parametric and versatile approach to efficient frequency conversion that uses second harmonic generation (SHG) to modify the dynamics of an optical parametric amplifier (OPA) to suppress back-conversion of the signal field to the pump. Numerical studies have recently shown this process, dubbed second harmonic amplification (SHA), can solve the OPA spatiotemporal efficiency problem by using SHG as a nonlinear loss channel for idler photons [31]. This was shown to generate dynamics similar to systems that use linear loss at the idler frequency where there is a damped oscillatory exchange of energy between the involved fields with full asymptotic convergence to the signal. However, by replacing linear loss with idler SHG, all of the otherwise lost energy is preserved in a coherent copropagating field at twice the idler frequency. Additionally, the constraint of working near a material resonance is alleviated as SHG can be simultaneously phase matched with OPA over a wide range of frequencies in many nonlinear materials using a number of techniques such as crystal and noncollinear angle tuning, temperature tuning, and quasi-phase matching [31, 18].

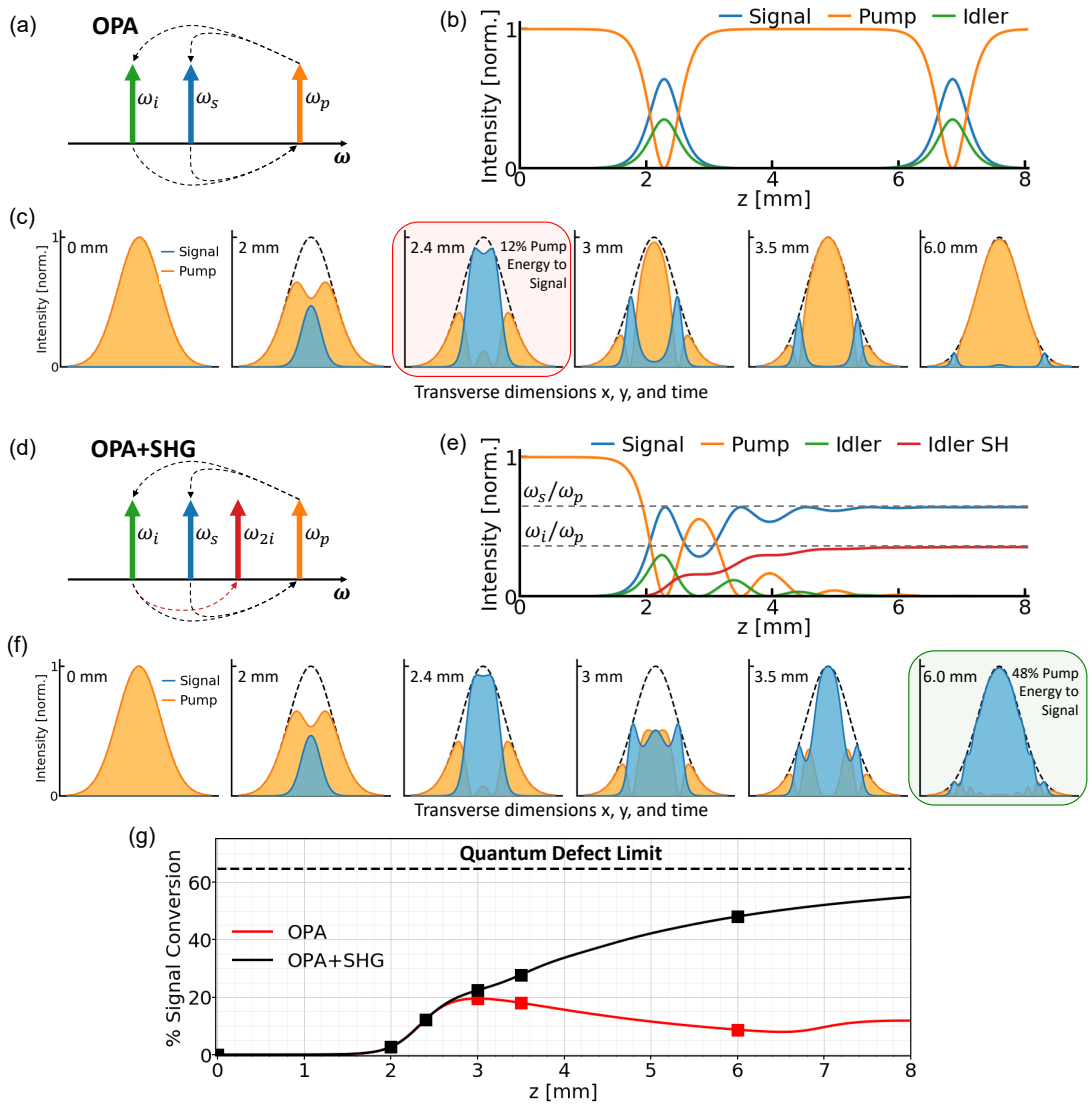

Figure 3.1: (a) Depiction of the cyclic energy flow between different frequency modes of conventional OPA. (b) Conventional OPA dynamics showing localized and periodic conversion of the pump field to the signal and idler fields. (c) Pump to signal conversion dynamics for a 1D slice of a Gaussian spatiotemporal profile where back-conversion limits the signal conversion efficiency to 12%. (d) Depiction of the energy flow between frequency modes of the OPA+SHG process. (e) OPA+SHG dynamics depicting damped oscillatory convergence of the pump field to the signal and idler SH fields. (f) The OPA conversion cycles are damped across the spatiotemporal profile enabling asymptotically full conversion to the signal field. (g) Signal energy conversion efficiencies for full 2+1D Gaussian spatiotemporal intensity distributions for OPA (red) and OPA+SHG (black).

3.1 THEORETICAL BACKGROUND

3.1.1 Conventional OPA

Figure 3.1 shows a comparison of the conventional OPA and OPA+SHG systems for monochromatic planewaves. In conventional OPA, the photons of a strong pump field at frequency ω_p undergo down-conversion into a weakly seeded signal field at frequency ω_s and an unseeded idler field at frequency ω_i (Fig. 3.1a). Due to conservation of energy, $\omega_p = \omega_s + \omega_i$ and the proportion of energy in the down-converted fields is given by ω_s/ω_p for the signal and ω_i/ω_p for the idler. This split in energy is a limitation on the maximum possible pump to signal energy conversion efficiency and is referred to as the quantum defect. The dynamics are cyclical with energy first flowing from the pump to the signal and idler fields, then returning to the pump through recombination of signal and idler photons to pump photons through back-conversion (fig. 3.1a,b). The short turning point in the dynamics where the pump field has fully converted to the signal and idler fields is known as saturation and is the typical operation point for most OPA implementations.

Fig. 3.1b implies that full conversion of the pump field to the signal and idler fields can be achieved if the device length is chosen correctly. However, OPA dynamics are highly dependent on the local intensity of the interacting fields which are generally nonuniform in space and time. Ultrafast lasers usually posses an intensity profile that is a 2+1D Gaussian spatiotemporal distribution. This creates a major limitation on the conversion efficiency of OPAs for realistic laser fields as no fixed device length can be chosen to achieve full conversion between fields. Figure 3.1c shows the conversion from pump to sig-

nal across a 1D slice of an initially Gaussian pump intensity distribution for a conventional OPA. The black dashed line indicates the point at which maximal conversion can be achieved. The center of the signal field can be seen to reach full conversion first before it begins to back-convert. Subsequently, the wings begin to convert, but not before most of the energy in the center of the signal field returns to the pump. The red curve in Fig. 3.1g shows the pump to signal energy conversion efficiency for conventional OPA. For a device length of 2.4 mm, chosen just before signficant back-conversion occurs, a mere 12% of the initial pump energy is transferred to the signal. Note that a higher conversion efficiency of 20% is possible, but not without sacrificing spacial beam quality by creating a ”doughnut beam” shape.

3.1.2 OPA+SHG System

In contrast to conventional OPA, when SHG of the idler wavelength occurs in simultaneity with the OPA interaction, idler photons are displaced to a coherent copropagating idler second harmonic (SH) field at frequency ω_{2i} (Fig. 3.1d). Crucially, the removal of idler photons inhibits back-conversion to the pump field, leading to the damped oscillatory behavior seen in Fig. 3.1e. This results in full asymptotic conversion of the pump field to the signal and idler SH fields with the final ratio of energy between the two determined by the quantum defect (grey dashed lines in Fig. 3.1e) These dynamics were recently described by a damped Duffing oscillator model with regions of over-damped and under-damped oscillation determined by the relative strength of the OPA and SHG processes [31]. Remarkably, the same model could be used to describe similar systems that use linear loss at the idler wavelength [60, 23, 96, 61], showing how

the behavior of phase matched SHG is analogous to nonlinear loss.

Fig. 3.1f shows the OPA+SHG conversion dynamics for 1D slices of Gaussian pump and signal intensity distributions. Initially, the behavior is that of conventional OPA (Fig. 3.1c), but after the first conversion cycle the impact of SHG is clear. Back-conversion is inhibited allowing full asymptotic conversion of the pump field to the signal across the entire Gaussian distribution. The signal profile is highly modulated at first, but takes on the shape of the pump profile as the interaction continues. The black curve in Fig. 3.1g is the pump to signal energy conversion efficiency which grows monotonically toward the quantum defect limit, showing an extended region of saturation akin to conventional laser amplifiers. For this hypothetical device, a deviation from the conventional OPA efficiency can be seen by 3 mm. By 6 mm, the conversion efficiency reaches 48%, a 4-fold increase over conventional OPA. Full conversion is possible, but the numbers chosen here are reflective of the experiment conducted below. Thus, the limitation on OPA efficiency due to the conversion cycles is lifted.

3.2 EXPERIMENTAL DEMONSTRATION

3.2.1 Experimental Setup

Our laser architecture is comprised of a 17 mJ Yb:YAG laser source (Amphos) which generates 1.03 μm pulses at a 10 kHz repetition rate. The front end up our laser architecture consists of YAG-based white light generation and amplification in two near-IR OPCPAs (BBO). To generate the pump laser for this

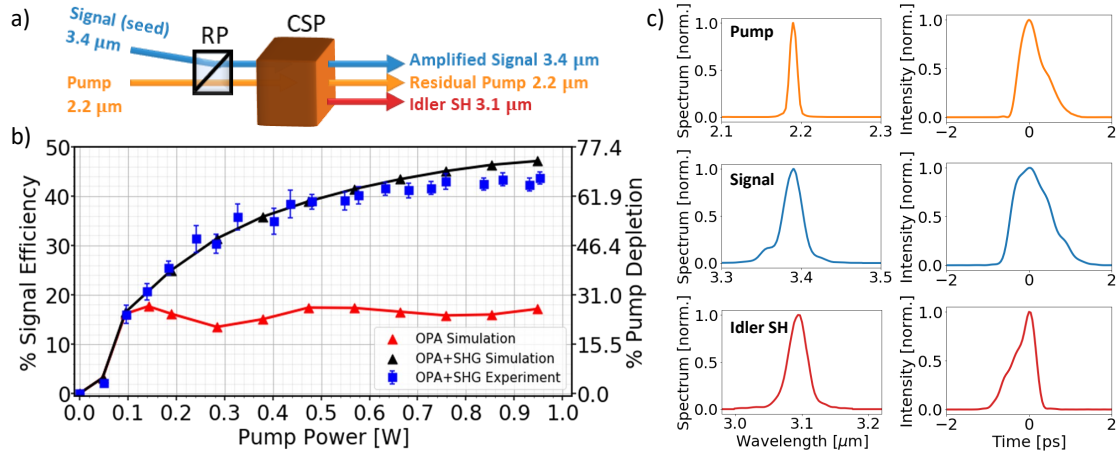

Figure 3.2: (a) Experimental setup: pump and signal beams are combined using a Rochon prism (RP) and enter the CSP crystal with near-collinearity. (b) Pump to signal conversion efficiency comparing the OPA+SHG experiment (blue squares) to simulated OPA+SHG (black triangles) and the equivalent OPA without SHG (red triangles). (c) Spectral and intensity measurements acquired using FROSt for the pump, signal, and idler SH at the full pump power.

experiment, we use a 4-f pulseshaper (Phasetech) to select the frequency and bandwidth of the near-IR pulses which are subsequently converted to the desired pump frequency in an adiabatic difference frequency converter. The pump pulses are then amplified to 100 μJ (1 W average power) using a periodically poled $LiNbO_3$ preamplifier and BiBo power amplifier. To generate the signal, we use a bandpass filter to select 790 ± 0.5 nm from the near-IR pulses which we convert to 0.7 nJ, 3.39 μm pulses in a parallel adiabatic frequency conversion stage.

Figure 3.2a shows our OPA + SHG experimental setup where 1 mm $1/e^2$ diameter, 0.6-ps, 100-μJ, 2.19-μm pump and 2 mm $1/e^2$, 1-ps, 0.7-nJ, 3.39-μm seed pulses are combined in a 6 mm $CdSiP_2$ (CSP) crystal using a Rochon prism to make them near-collinear. CSP is a uniaxial material relevant to mid-infrared applications in frequency conversion. It is known to have a broad phase-matching bandwidth for Type-I OPA pumped near 2 μm [85, 56]. Our

CSP crystal is cut at 45 degrees and at 43 degrees, we achieve simultaneous phase matching for downconversion of our 2.19 µm pump to a 3.39 µm signal and 6.2 µm idler and SHG of the idler to a 3.1 µm idler SH. The CSP crystal is AR-coated and has roughly 96% transmission on each facet measured using a 1 mm CSP window with identical coating.

At the output of the CSP crystal, reflections of the beams from a CaF_2 beam sampler are imaged with a CaF_2 lens in a 2F configuration to a bolometer camera (DataRay) and separated by polarization using a Wollaston prism. To measure the power of each beam after the OPA + SHG nonlinear interaction, the beam sampler is removed and various bandpass filters are used (Thorlabs 2250±500 nm, Thorlabs 3500±500 nm, and Andover 3050±100 nm) to isolate the signal, pump, or idler SH. The experiment is optimized with the beam sampler in place so that the signal power and beam images can be viewed simultaneously. The signal alignment, crystal angle, and temporal overlap can then be adjusted to optimize for signal power and beam quality.

3.2.2 Results

The pump to signal energy conversion efficiency internal to the device as a function of input pump power is shown in Fig. 3.2b. The experimentally measured (blue squares) and simulated (black triangles) data for the OPA + SHG process are in good agreement with a clear trend of monotonically increasing efficiency due to inhibited back-conversion. This creates an extended region of saturation as predicted, and the reduction in the noise of the measurements is a consequence of pushing further into saturation. The maximum efficiency achieved is

43.6% corresponding 41.6 μJ of energy in the signal field and 48 dB energy gain. The measurements were confirmed by measuring the pump depletion which reaches 67.5% at the full input pump power. A slight deviation in conversion efficiency between the experimental and simulated results is observed at higher pump powers which signifies the onset of back-conversion. This is described in more detail in the discussion of the beam profiles below.

The OPA+SHG experimental results are compared to conventional OPA in Fig. 3.2b (red triangles) by performing identical simulations with coupling to the idler SH prohibited. In this case, the pump to signal energy conversion efficiency does not exceed 18% with saturation happening around 100 mW of pump power yielding 2.9 μJ of signal or 36 dB energy gain.The efficiency then undergoes multiple oscillations as energy is exchanged across the pump and signals spatiotemporal coordinates. It is also important to note that because this OPA achieves lower gain, the efficiency would be further reduced by an OPA optimized to operate at higher gain. This makes it eminently clear that the OPA conversion efficiency is enhanced several fold by the addition of simultaneously phase matched idler SHG. Further, for identical operating conditions, the OPA+SHG device can be pushed to more than an order of magnitude higher gain which, in some cases, could eliminate the need for a pre-amplifier.

The pump, signal, and idler SH temporal profiles were measured using frequency resolved optical switching (FROSt), as seen in Fig. 3.2c. FROSt is a recently demonstrated phase-matching-free characterization technique [54, 59]. The input pump duration was measured at 0.64 ps and we measured 1.04 ps for the signal and 0.58 ps for the idler SH at the full pump power. The pump pulse was not compressed to its transform limit and has a large amount of TOD ac-

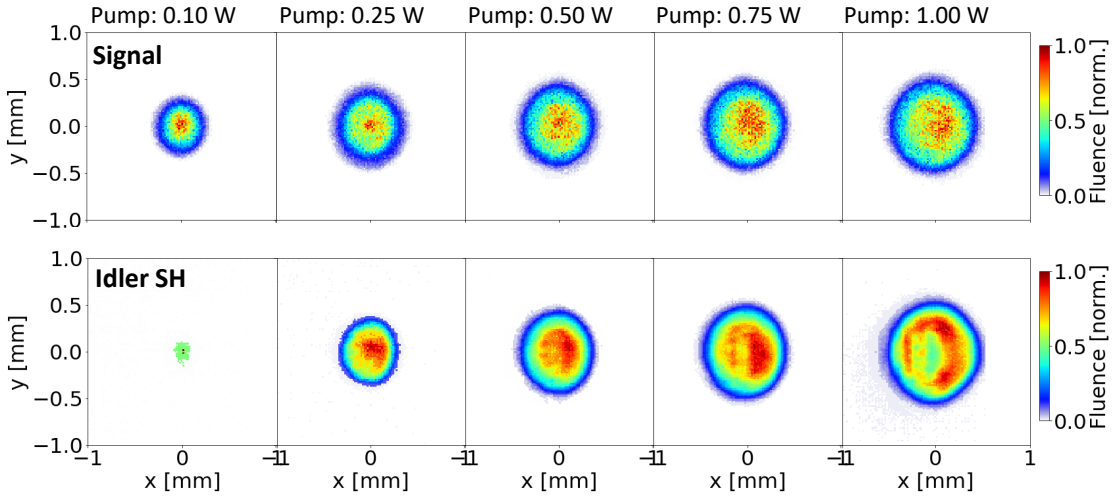

Figure 3.3: Experimental beam measurements for the signal and idler SH as the input pump power is increased.

counting for its asymmetric shape. This shape can be seen to be imparted to the signal pulse as well as some material dispersion accounting for the increased duration. The idler SH is well into back conversion for this measurement as discussed below and so the shape can not be directly compared to that of the pump and signal.

The spatial evolution of the signal and idler SH beams as the pump power is increased can be seen in Fig. 3.3. At 0.1 W of pump power, the signal is just reaching saturation where the conventional OPA would operate and the idler SH is just starting to be generated. By 0.25 W of pump power, the signal has already undergone a conversion cycle. A ring-shaped feature can be observed at the edge of the beam and a second conversion peak is forming at the center of the beam. At this point, conversion of the idler to the idler SH has become substantial. As the pump power approaches 1 W, both the signal and idler profiles fill out to the full 1 mm $1/e^2$ beam diameter of the initial pump beam.

An asymmetric hole can be seen forming on the left side of idler SH image at

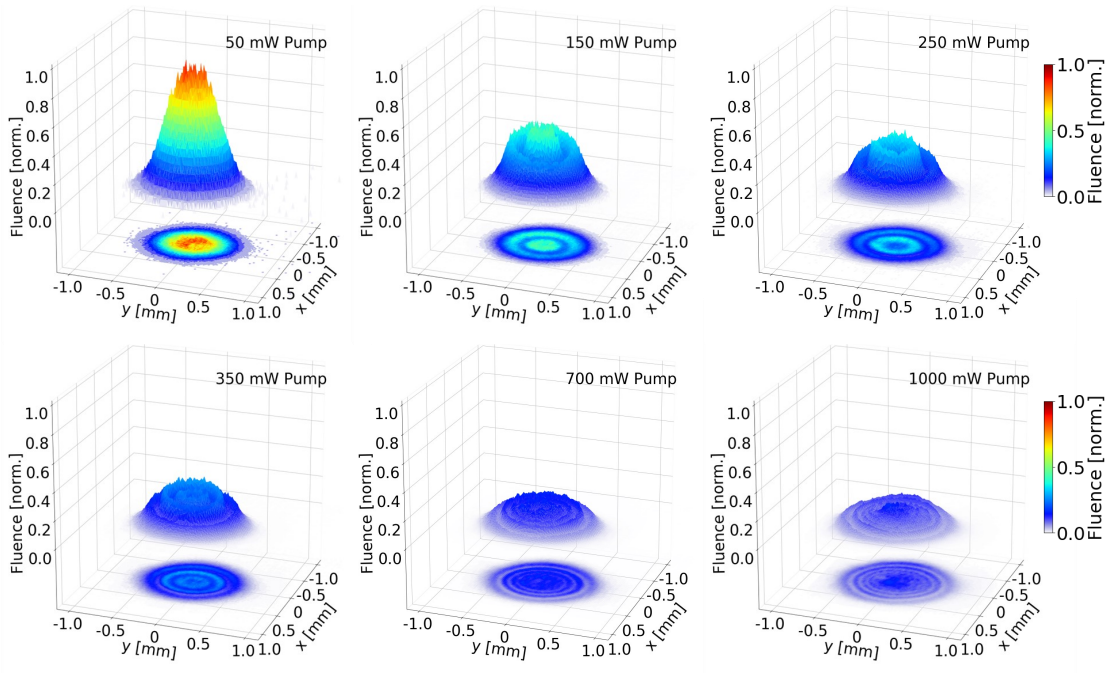

Figure 3.4: Pump beam profile measured after the CSP crystal for increasing input pump power revealing the damped oscillatory nature of the OPA+SHG dynamics.

large pump power. This is an indication that the spatial walk-off of the idler SH is leading to eventual phase mismatch of the SHG process and back-conversion of the idler SH field to the idler. Once back-conversion of the idler SH begins to occur, there is still significant enhancement of the signal beam as several damped conversion cycles are undergone before significant back-conversion occurs [31]. We believe this effect accounts for the deviation between the experimental and simulated data in Fig. 3.2b. Further, the effects of beam walk-off can be mitigated by going to larger beam diameters and increasing the pump power. However, in this experiment, we were limited to 1 W of pump power.

Fig. 3.4 shows residual pump beam with increasing power through the device. This is the first ever observation of the damped oscillatory dynamics of OPA+SHG, confirming the predictions by [31]. A modulated ring pattern can

be seen forming across the pump spatial profile. These are evidence that the oscillatory exchange of energy with the signal and idler is damped out, leading to simultaneous conversion to the signal and idler SH across successively larger radial coordinates. The amplitude of these modulations decrease with higher pump power leading to a cleaner signal beam. As discussed in [31], the exact modulation frequency depends on the relative strength of the SHG and OPA processes. Here, the oscillations are underdamped, but a different choice of system parameters or through quasi-phase matching, the SHG process could become strong enough to reach the overdamped regime. In this regime, there is a unidirectional conversion between all waves, and at the critical damping point, full conversion happens rapidly, requiring a mere half-conversion cycle [31].

3.3 DISCUSSION

There are a number of advantages associated with implementing efficient frequency conversion and amplification with parametric processes in the absence of material gain or loss. First, there are many degrees of freedom that can be leveraged to achieve simultaneous phase matching of OPA and SHG. Prior investigations have shown this to be possible over a wide range of existing nonlinear media (such as BBO, CSP, and $LiNbO_3$) using non-collinear geometries [18] and quais-phase matching (QPM) [31]. Non-collinearity can provide a wide frequency tuning range in a single crystal and is a route toward tunable and efficient downconversion of high average power 1- and 2-μm solid-state diode-pumped lasers due to the large aperture of available bulk nonlinear media. QPM can enable arbitrary phase matching within the transparency range of

materials such as $LiNbO_3$, KTP, and GaAs provided manufacturing constraints and energy conservation between frequencies are observed. A further advantage of QPM is the ability to tune the relative nonlinear strength of OPA and SHG through the poling structure in order to tune the damping parameter toward the critical damping regime. This could enable rapid conversion without the oscillatory dynamics of the underdamped regime. Yet to be explored are additional phase matching techniques such as temperature tuning.

A unique advantage of using a nonlinear parametric process to induce lossy behavior is that the lost idler energy is preserved in the copropagating idler SH field and can be reused to act as the pump in a subsequent signal amplification stage. This is a route to overcoming the quantum defect which is another fundamental limitation on OPA efficiency described above. Cascading such stages could drastically improve the efficiency of long-wave IR generation where the quantum defect limits maximum conversion efficiency to a few percent.

CHAPTER 4

HERMITIAN NONLINEAR WAVE MIXING CONTROLLED BY A PT-SYMMETRIC PHASE TRANSITION

4.1 BACKGROUND: NON-HERMITIAN PHYSICS

Over the past two decades, the unique physics that emerge from open non-Hermitian systems have enabled a multitude of new device capabilities that overcome the limitations of their closed Hermitian equivalents [25, 74, 24, 75]. These capabilities arise largely through the dynamics that emerge near exceptional points in the non-Hermitian system eigenspectra, at which both eigenvalues and eigenvectors coalesce and regions of broken and unbroken PT-symmetry are demarcated under conditions of balanced gain and loss. Many device functionalities including single-mode lasing [40], unidirectional invisibility [57, 27], asymmetric mode-switching [34, 20, 44], exceptional point enhanced sensitivity [39, 15, 50], and improved efficiency and bandwidth of parametric amplification [60, 23, 96, 61] have been proposed or realized through careful engineering of gain and loss.

However, the need for incoherent gain and loss creates practical limitations in non-Hermitian devices. It limits efficiency, creates inflexibility in the gain and loss bands, and produces undesirable signal-to-noise characteristics near exceptional points [53, 51, 14]. To circumvent these limitations, recent works have investigated coherent interactions that can be used to the same effect. For instance, nonlinear parametric wave-mixing processes – where there is coupling between modes of different frequency or polarization – can be used to coherently add and remove energy from bosonic subsystems, thereby inducing non-

Hermitian behavior without an incoherent exchange of energy with the medium [68, 41, 95, 7, 93, 81, 82]. In these works, strong laser fields act as a reservoir of photons that can be exchanged with a subsystem. While these interactions usually take place in an approximately linear regime, in which the reservoir is effectively unperturbed, they have recently been extended to the nonlinear gain saturation regime where appreciable energy is added or removed from the strong driving fields [81, 82].

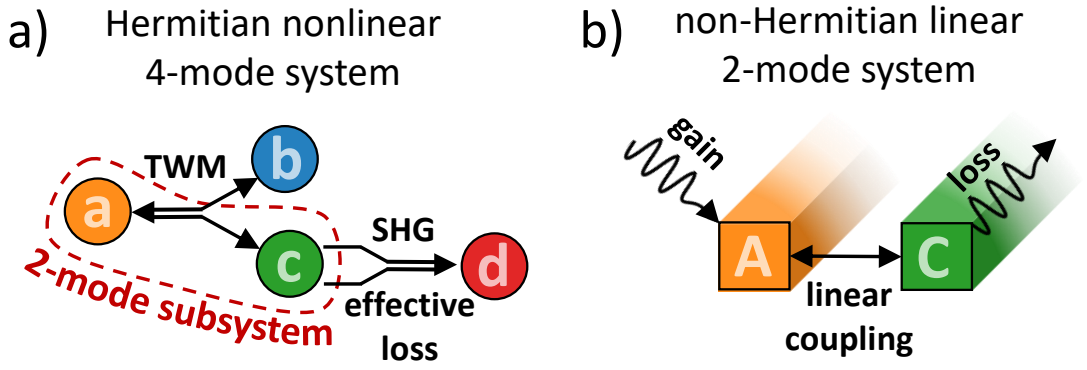

Figure 4.1: (a) A Hermitian system consisting of hybridized TWM and SHG can be represented by a 2-mode subsystem with an effective loss channel. This subsystem behaves analogously to (b) a non-Hermitian linear 2-mode system (e.g., coupled waveguides) with balanced gain and loss.

4.2 TWM+SHG SYSTEM

Here we investigate the back-action of non-Hermitian subsystems on the behavior of the coherently coupled driving fields in such systems and find new phenomena. Our platform is simply parametric three-wave mixing (TWM) hybridized with second harmonic generation (SHG) (Fig. 4.1a), where the SHG provides an effective loss channel on one of the fields. In this Hermitian, 4-mode, nonlinear wave mixing system, we find a 2-mode subsystem that exhibits a PT-symmetric phase transition in analogy to coupled waveguides with

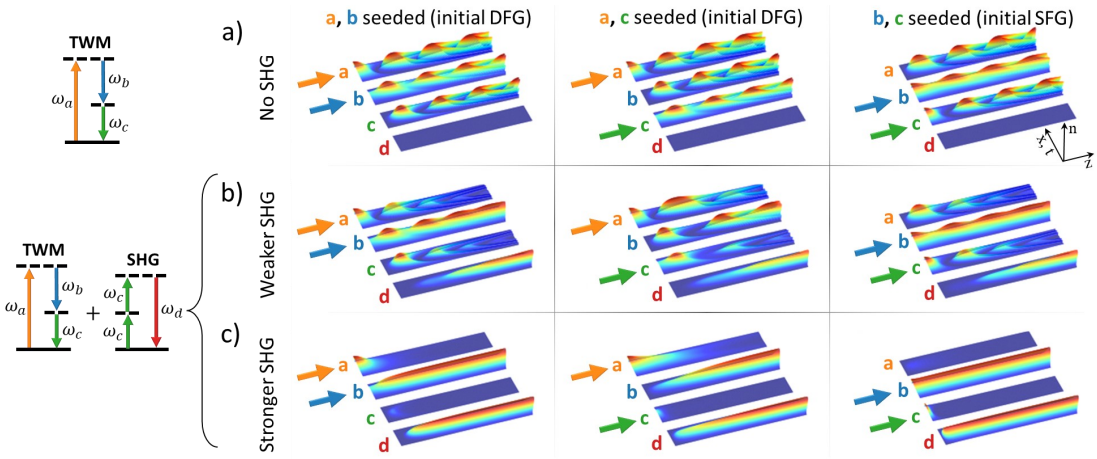

Figure 4.2: (left) Virtual energy level diagrams depicting (right) energy-conserving photon exchanges with only two of the fields a, b, and c seeded (indicated by the arrows) for (a) phase-matched conventional TWM, where an oscillatory exchange of power occurs; and (b,c) when SHG ($2\omega_c = \omega_d$) is simultaneously phase matched. In (b), SHG is weak compared to TWM leading to a damped oscillatory conversion with asymptotic transfer to fields b and d. In (c), SHG is strong compared to TWM, inhibiting SFG and leading to a unidirectional transfer of energy to fields b and d. We note that the parameter η_∞, as defined later, is held constant across columns in each row, implying differences in material constants and/or photon frequencies.

balanced gain and loss (Fig. 4.1b). Back-action on the enclosing system results in all modes evolving according to the subsystem PT-symmetric phase. This discovery offers exciting new avenues for extending applications of non-Hermitian physics to systems where high efficiency and energy conservation is desired – a regime precluded for non-Hermitian devices due to their inherent lossy nature and/or requirement of an external gain source. In this case, breaking the cyclic nature of TWM allows for a unidirectional flow of photons that enables efficient frequency conversion.

Conventional TWM interactions can be described as a cyclic exchange of photons between a higher frequency field at ω_a with two fields at lower frequencies ω_b and ω_c such that $\omega_a = \omega_b + \omega_c$. This one-to-two photon exchange

is mediated by the quadratic nonlinear polarizability of a noncentrosymmetric medium and is energy-conserving when all frequencies are far from any material resonances [2]. SHG is the degenerate case of TWM where the two lower frequencies are equal. In this paper, we consider the process $\omega_c + \omega_c = \omega_d$. For an efficient exchange of photons between fields, coherence between propagating and nonlinear polarization fields of the material must be maintained at each frequency. This occurs when the wave-vector mismatch, $\Delta\vec{k}_{abc} = \vec{k}_a - \vec{k}_b - \vec{k}_c$ for TWM and $\Delta\vec{k}_{dcc} = \vec{k}_d - 2\vec{k}_c$ for SHG, vanishes (known as perfect phase matching) [35].

4.2.1 Dynamics

For monochromatic plane waves, this hybrid system of TWM and simultaneous SHG can be modeled by four coupled evolution equations derived from Maxwell's equations. Hybridization is made possible by perfect phase matching of both processes (which can be achieved under various conditions [31]), resulting in:

$$d_z u_a(z) = i\Gamma_{abc} u_b(z) u_c(z) \tag{4.1a}$$

$$d_z u_b(z) = i\Gamma_{abc} u_a(z) u_c^*(z) \tag{4.1b}$$

$$d_z u_c(z) = i\Gamma_{abc} u_a(z) u_b^*(z) + 2i\Gamma_{dcc} u_d(z) u_c^*(z) \tag{4.1c}$$

$$d_z u_d(z) = i\Gamma_{dcc} u_c^2(z). \tag{4.1d}$$

The $u_j(z)$ are non-dimensional electric field amplitudes for $j \in \{a, b, c, d\}$ where $\left|u_j(z)\right|^2 = n_j(z)$ is the photon flux density in the jth field normalized by the total initial photon flux density, which we refer to as the fractional photon flux density of the jth field. Γ_{abc} and Γ_{dcc} are the drive strengths of the TWM and

SHG processes, respectively. (Definitions in terms of complex electric field amplitudes $A_j(z)$, refractive indices, n_j, and nonlinear coefficient, d_{eff}: $k_j = \omega_j \mathrm{n}_j/c$, $u_j(z) = \sqrt{2\mathrm{n}_j\epsilon_0 c/\hbar\omega_j F_0}A_j(z)$ where $F_0 = \sum_j 2\mathrm{n}_j\epsilon_0 c\,|A_j(z=0)|^2/\hbar\omega_j$ is the total initial photon flux. $\Gamma_{ijk} = 1/p\sqrt{\hbar\omega_i\omega_j\omega_k d_{ijk}^2 F_0/2\mathrm{n}_i\mathrm{n}_j\mathrm{n}_k\epsilon_0 c^3}$ where p relates to the degeneracy of the process ($p = 1$ for TWM and $p = 2$ for SHG). d_{ijk} is proportional to the tensor element of the quadratic electric susceptibility for the specific field polarizations of the three mixing fields i, j, and k.

Conventional TWM of waves with Gaussian transverse (spatial or temporal) mode profiles is depicted in Fig. 4.2a. Conventional TWM takes place when $|\Delta k_{abc}| = 0$ and $|\Delta k_{dcc}| >> 0$, and in this case, Eqs. 4.1c,d reduce to $d_z u_c = i\Gamma_{abc}u_a u_b^*$ and $d_z u_d = 0$. For any combination of two fields initially nonzero, we observe evolution that cycles between the processes of difference frequency generation (DFG) ($\omega_a \rightarrow \omega_b, \omega_c$), and sum frequency generation (SFG) ($\omega_b, \omega_c \rightarrow \omega_a$). Due to the nonlinear dependence on field amplitudes in Eqs. 4.1, the periodicity of the conversion cycle varies across the transverse coordinate, leading to inhomogeneous conversion dynamics and a fundamental limitation on the conversion efficiency of the device as discussed in [31].

When SHG is coupled to one of the lower frequency fields by satisfying $\Delta\vec{k}_{dcc} = 0$, SFG is inhibited and two distinct phases of dynamics are observed (Fig. 4.2b,c). In both phases, we observe that asymptotically full conversion from modes a and c to b and d takes place independent of the initial local intensity, effectively homogenizing the modal transfer between the input and output fields. However, when TWM is strong in comparison to SHG (Fig. 4.2b), the TWM is characterized by damped oscillations, and in contrast, when SHG is strong compared to TWM (Fig. 4.2c), SFG is fully inhibited and the conver-

sion is monotonic. In the following, we show analytically how the behavior of this closed Hermitian system and the emergence of these distinct phases results from underlying non-Hermitian physics.

4.2.2 SHG as a Form of Loss

To begin this discussion, we point out that phase-matched SHG differs from most TWM interactions, in that the conversion dynamics are not cyclic. The displacement of photons to the second harmonic (SH) field is monotonic and irreversible, thus sharing a primary feature of loss due to contact with a thermal bath. This was pointed out in the context of parametric amplification [31], in which SHG was observed to induce behavior normally associated with loss [60, 23, 96, 61]. Yet, unlike a heat bath, the coupling between a wave and its SH is coherent, and unidirectional flow is a consequence of a vanishing polarization field at both the fundamental and SH frequencies. Moreover, since the growth of the SH field is quadratic in the fundamental (Eq. 4.1d), the irreversibility of flow is even insensitive to pi phase modulations in the fundamental field [31]. In the hybridized process in Fig. 4.2b,c, this insensitivity enables a unidirectional flow of energy to the SH field even as the fundamental field undergoes conversion cycles. Thus, even when taken to full conversion, the SHG provides a loss channel for the TWM system by which we might expect the emergence of an exceptional point that demarcates regions of broken and unbroken PT-symmetric phases.

4.3 ANALYSIS

4.3.1 Photon Exchange Rates & Manley Rowe Equations

To begin the analysis, we derive from Eqs. 4.1 a set of equations that describe the rate at which photons are added and removed from each field by a given nonlinear interaction (TWM or SHG). These are derived by computing derivatives of each n_j:

$$d_z n_a(z) = -\rho_{abc}(z) \tag{4.2a}$$

$$d_z n_b(z) = \rho_{abc}(z) \tag{4.2b}$$

$$d_z n_c(z) = \rho_{abc}(z) - 2\rho_{dcc}(z) \tag{4.2c}$$

$$d_z n_d(z) = \rho_{dcc}(z) \tag{4.2d}$$

where $\rho_{abc}(z) = 2\Gamma_{abc} Im\{u_a^*(z)u_b(z)u_c(z)\}$ and $\rho_{dcc}(z) = 2\Gamma_{dcc} Im\{u_d(z)(u_c^*(z))^2\}$ represent the rate at which photons are added (removed) from each field by TWM and SHG, respectively. We have chosen the sign convention such that $\rho_{abc}(z) > 0$ represents DFG and $\rho_{abc}(z) < 0$ represents SFG. It is always the case that $\rho_{dcc}(z) \geq 0$ since photons can only move unidirectionally into field d from field c as discussed above. From these equations it is simple to derive a set of linearly independent relationships known as the Manley-Rowe equations that define conserved quantities in terms of photon flux:

$$N_1 = n_{a,0} + n_{b,0} = n_a(z) + n_b(z) \tag{4.3a}$$

$$N_2 = n_{a,0} + n_{c,0} + 2n_{d,0} = n_a(z) + n_c(z) + 2n_d(z), \tag{4.3b}$$

where the $n_{j,0}$ are the initial fractional photon flux densities and $n_{d,0} = 0$ for the system under consideration. Thus, as the fields evolve, the number of photons

in the *a*-*b* and *a*-*c*-*d* subsystems are constrained by the initial fractional photon flux density of the seeded fields. From this constraint and the unidirectionality of SHG, we can infer $n_b(z \to \infty) = N_1$ and $n_d(z \to \infty) = N_2/2$ while $n_a(z \to \infty) = n_c(z \to \infty) = 0$ which captures the asymptotic behavior seen in Fig. 4.2b,c.

4.3.2 Identifying the Non-Hermitian Subsystem

We now seek to understand the intermediate dynamics seen in Fig. 4.2b,c in terms of non-Hermitian physics. Since Eq. 4.3b suggests SHG acts directly to remove photons from fields *a* and *c*, we direct our attention to the *a*-*c* subsystem before turning our attention to the full system. Typically, an investigation of non-Hermitian physics involves computation of the eigenspectra for a linearly coupled subsystem with gain and loss. While nonlinear TWM systems have long been investigated in approximately linear regimes by way of undepleted field approximations or adiabatic elimination, here we take a new approach that allows us to investigate the non-Hermitian features in the fully nonlinear regime without approximation. This analysis requires *a priori* knowledge of the evolution of fields *b* and *d* by first solving the wave mixing equations (Eqs. 4.1) numerically. We can intuitively think of field *b* as contributing to a propagation varying coupling constant $\kappa_{ac}(z) = \Gamma_{abc} u_b(z)$ for fields *a* and *c* while $\gamma_{cc}(z) = \Gamma_{dcc}|u_d(z)|$ represents a monotonically growing two-photon loss on field *c*. We then cast the *a*-*c* subsystem (Eqs. 4.1a,c) in a frame where the loss on mode *c* is balanced by equivalent gain on mode *a* by performing the gauge transformation $[u_c', u_a'] = [u_c, u_a] e^{\int_0^z \gamma_{cc}(z')dz'}$. Over length scales where $|\Delta k_{abc} z|$ and $|\Delta k_{dcc} z| \ll \pi$, we find this transformation provides a powerful analytic tool for identification of parameters that dictate the occurrence of phase transitions within the nonlin-

ear system.

Substituting these coordinates into Eqs. 4.1a and 4.1c, we can write the coupled *a*-*c* subsystem equations in the simplified Hamiltonian form,

$$-i\frac{d}{dz}\begin{bmatrix} u_c'(z) \\ u_a'(z) \end{bmatrix} = \begin{bmatrix} i\gamma_{cc}(z) & \kappa_{ac}^*(z) \\ \kappa_{ac}(z) & -i\gamma_{cc}(z) \end{bmatrix}\begin{bmatrix} u_c'(z) \\ u_a'(z) \end{bmatrix}. \tag{4.4}$$

The propagation-dependent Hamiltonian of this system is given by $H_{ac}(z) = \vec{g}(z)\cdot\vec{\sigma}$ where $\vec{g}(z) = (Re\{\kappa_{ac}(z)\}, Im\{\kappa_{ac}(z)\}, i\gamma_{cc}(z))$ expresses the coupling and loss of the system and $\vec{\sigma}$ is the Pauli vector. This Hamiltonian is non-Hermitian except in the $\gamma_{cc}(z) = 0$ case, which represents conventional TWM without SHG. It is also easy to check $H_{ac}(z)$ commutes with the parity-time operator by computing $[H_{ac}(z), PT] = 0$ with parity inversion of fields a and c given by $P = \sigma_x$ and time reversal given by complex conjugation ($TuT^{-1} = u^*$).

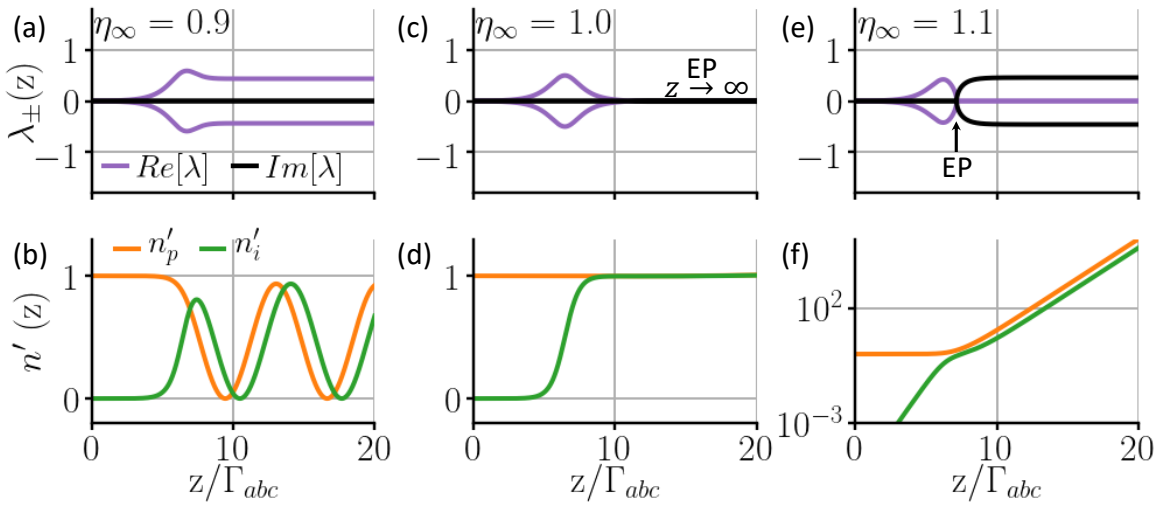

Figure 4.3: Numerical solutions for *a*-*c* subsystem dynamics in the gauge transformed frame for (a,b), $\eta_\infty < 1$, having power oscillations and purely real eigenvalues for all z; (c,d), $\eta_\infty = 1$, in which fields a and c coalesce as the system asymptotically approaches the exceptional point; and (e,f), $\eta_\infty > 1$, showing exponential growth and a transition from purely real to purely imaginary eigenvalues at the exceptional point. All cases: $n_{b,0} = 10^{-5}$ and $n_{a,0} = 1 - n_{b,0}$.

A local eigenspectra analysis of $H_{ac}(z)$ yields propagation dependent eigen-

values $\lambda_{\pm}(z) = \pm\sqrt{\vec{g}(z)\cdot\vec{g}(z)} = \pm\sqrt{|\kappa_{ac}(z)|^2 - |\gamma_{cc}(z)|^2}$ where an exceptional point occurs when the coupling and loss are equivalent, or in physical terms, when the SHG and TWM processes act with equal strength on the subsystem. We introduce the state parameter $\eta(z) = \sqrt{|\gamma_{cc}(z)|/|\kappa_{ac}(z)|}$ which quantifies the relative strength of loss due to SHG to coupling due to TWM. We find the local right eigenvectors depend solely on this new parameter: $\vec{v}_{\pm}(z) = 1/\sqrt{2}[1, i\eta(z) \pm \sqrt{1-\eta(z)^2}]^T$. An exceptional point exists at $\eta = 1$, where the eigenvalues and local right eigenvectors coalesce. When $\eta(z) < 1$, coupling by TWM is the dominant process and the subsystem is PT-symmetric with purely real eigenvalues. When $\eta(z) > 1$, loss of photons by SHG is dominant and PT-symmetry is broken, resulting in purely imaginary eigenvalues. Whether the system converges to the broken or unbroken PT-symmetric phase is determined by the steady state parameter $\eta_\infty \equiv \eta(z \to \infty) = \Gamma_{dcc}/\Gamma_{abc}\sqrt{N_2/2N_1}$. For values of $\eta_\infty < 1$, fields a and c will forever engage in bidirectional power exchange via SFG/DFG conversion cycles (Fig. 4.3a, b). When $\eta_\infty > 1$, PT-symmetry is broken at finite z, leading to a complete elimination of the bidirectional exchange of power between fields a and c that is characteristic of TWM (Fig. 4.3e, f). Thus, the conditions for PT-symmetry breaking are determined by the relative drive strength of the SHG and TWM processes and by the initial conditions through the conserved quantities of Eqs. 4.3.

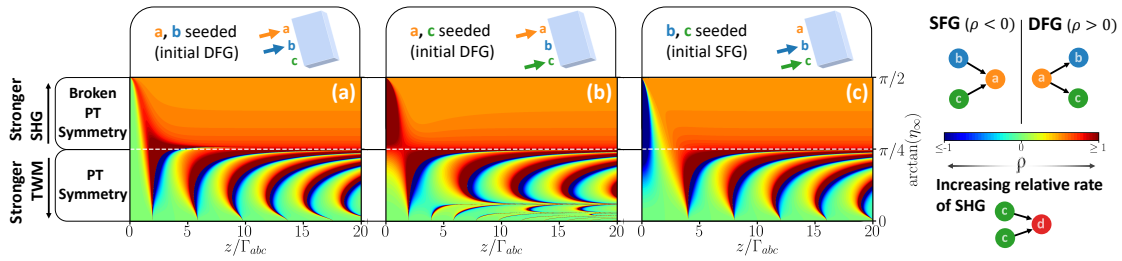

Figure 4.4: Gauge-invariant parameter $\rho(z)$ (color map) for initial conditions corresponding to DFG with (a) fields a and b seeded, (b) fields a and c seeded, and (c) SFG with fields b and c seeded. A white dashed line corresponding to $\eta_\infty = 1$ demarcates a sudden transition in behavior corresponding to the PT-symmetric phase of the a-c subsystem. The colorscale is truncated at ± 1 for clarity.

4.3.3 Influence of the Non-Hermitian Subsystem on the Full Hermitian System

So far, we have revealed how non-Hermitian physics emerges in the a-c subsystem of any TWM process as a consequence of simultaneously phase-matched SHG. Our approach also allows an exact analysis over the full range of power exchange dynamics, rather than employing a linearized model that excludes the coherence between the subsystem and external fields. Thus, we can analyze another interesting feature: the back-action of the non-Hermitian a-c subsystem on the external fields b and d. In the following analysis, we investigate how the abrupt transition in PT-symmetric phase in the non-Hermitian 2-mode a-c subsystem imprints on the 4-mode Hermitian system, leading to the dynamics in Fig. 4.2.

A compact representation of the 4-mode system dynamics is given by the real parameter $\rho(z) = \rho_{dcc}(z)/\rho_{abc}(z) = \eta\sqrt{n_c'/n_a'}$. Its magnitude quantifies the relative rate of photons being exchanged by SHG compared to TWM. At its extrema, $|\rho(z)| \in \{0, \infty\}$, only TWM or SHG occur, respectively. The sign of $\rho(z)$

represents the direction of TWM photon exchange, with $\rho(z) > 0$ corresponding to DFG and $\rho(z) < 0$ corresponding to SFG. Since this parameter is defined as a ratio, it is gauge invariant, and thus can be interpreted in terms of either the 2-mode *a*-*c* subsystem or the full 4-mode system.

Figure 4.4 depicts the photon exchange dynamics for three representative cases of TWM and in each case exhibits an abrupt phase transition in the dynamics of the closed Hermitian system. This phase transition is demarcated by the white dashed line at $\arctan(\eta_\infty) = \pi/4$ (i.e., $\eta_\infty = 1$). When $0 \leq \arctan(\eta_\infty) < \pi/4$, the *a*-*c* subsystem always remains PT-symmetric and there is a perpetual oscillation in the relative rate of SHG and TWM interactions with the TWM process periodically switching between DFG and SFG, as seen in Fig. 4.2b. In this phase, the dynamics of photon exchange are highly dependent on the specific system parameters. However, when $\pi/4 \leq \arctan(\eta_\infty) < \pi/2$, the exceptional point is crossed at finite z and we see rapid convergence to dynamics involving only DFG and SHG at a fixed rate, leading to the monotonic growth of fields *b* and *d*, independent of which two of the TWM fields are initially seeded, as seen in Fig. 4.2c. Thus, we see how the abrupt transition in the PT-symmetric phase of the non-Hermitian 2-mode subsystem is imprinted on the enclosing Hermitian 4-mode system. In fact, the exact relative rate of DFG and SHG reached in equilibrium, $\rho(z \to \infty) = \eta_\infty^2 - \sqrt{\eta_\infty^4 - \eta_\infty^2}$, depends only on the *a*-*c* subsystem state parameter η_∞, and is independent of the initial behavior of the TWM system.

4.4 DISCUSSION

These findings have a number of interesting implications. We have shown that the evolution behavior of a Hermitian wave-mixing system is tied to non-Hermitian behavior of an enclosed subsystem, even through a full nonlinear power exchange. In non-Hermitian nonlinear wave mixing systems, it has been established that conversion between modes can be homogenized across their transverse profiles, linearizing the input-output behavior. This is important, as it solves the longstanding problem of inefficient frequency conversion [60, 23, 96, 61, 31]. That this can be achieved without any real loss or coupling to a thermal bath – enabled rather by coherent coupling to a co-propagating wave – can circumvent other problems. As pointed out previously, thermal loading can be avoided [31] and phase noise improved [81, 82], and the loss band can be chosen by phase-matching technique rather than being tied to material or structural resonances. Moreover, in our system, the photons displaced from the enclosed subsystem are preserved in a coherent field that can be used in subsequent applications. All of these are significant capabilities for advancing frequency conversion technology that can be important for laser science and integrated photonics. More generally, the use of non-Hermitian physics to explicitly control an enclosing Hermitian system, as shown here, may have broader applicability and importance where energy efficiency and sustainability are of concern.

[1]

[1]This chapter is derived from [30] with small changes.

CHAPTER 5

ADIABATIC FREQUENCY CONVERSION

Generating octave-spanning coherent bandwidths and compressing them to their transform-limits are among the most challenging aspects of optical systems used for ultrafast spectroscopy and control of matter, especially at the single-cycle limit. Typically, octave-spanning bandwidths are generated using super-continuum generation, noncollinear or frequency domain optical parametric amplification [13, 86], coherent beam synthesis [63], nonlinear multimode mixing in gas-filled hollow core fibers [77], and adiabatic frequency conversion [91, 65]. In particular, adiabatic frequency conversion is a promising new technique that has demonstrated single-cycle pulse generation in the mid-infrared while preserving the phase properties and absolute bandwidth of the input pulse. However, as absolute bandwidths grow large, precise dispersion management in these systems plays an increasingly important role; transmission through even a few millimeters of an optical device can become a limiting technical factor. Standard compressors using bulk material, gratings, and prisms can offset large amounts low-order dispersion, but struggle to mitigate higher-order dispersion and can even exacerbate it.

To address the challenge of higher-order dispersion, modern octave-spanning systems have successfully incorporated multiple double-chirped mirror pairs or programmable dispersive filters [63] in combination with the standard approaches outlined above. However, increasingly complex dispersion management schemes impact the cost, stability, flexibility, and construction time of ultrafast laser architectures. A greatly simplified single-cycle mid-IR source of CEP-stable transients could significantly extend the boundaries of ultrafast

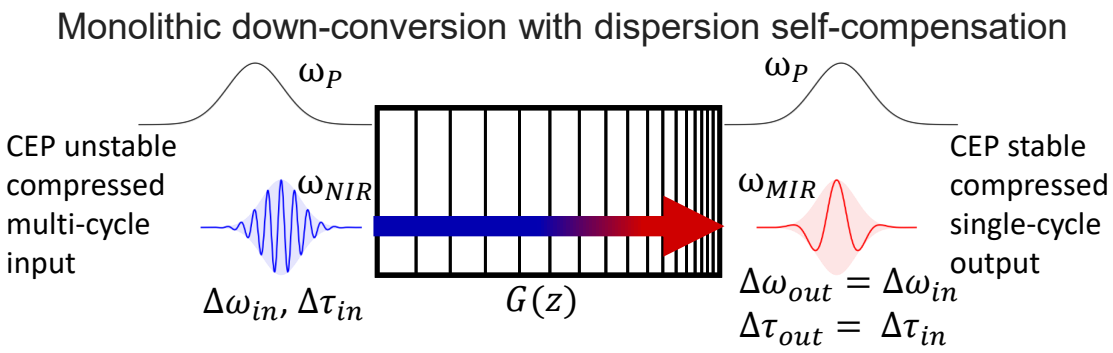

Figure 5.1: Self-dispersion managed ADFG concept: a compressed multi-cycle near-IR wave undergoes bandwidth and phase-conserving adiabatic down-conversion to a compressed, CEP-stable, single-cycle mid-IR pulse in a chirped QPM grating with a local poling frequency G(z) designed to impart zero net GDD.

science for applications including electronics at optical clock rates [52], attosecond science [17], and field-resolved detection of plasmonics [28].

Additionally, standard experiments in 2DIR spectroscopy require interferometrically stable identical pulse pairs and more advanced experiments require the ability to impress differences on these pairs such as relative phase, amplitude, and spectral content. An interferometer produces identical mid-IR pulse pairs but lacks stability and introduces timing jitter. A spatial light modulator inside a grating pair or an acousto-optic programmable dispersive filter (AOPDF) would enable arbitrary shaping of post-generation pulses; however, such devices are usually limited to sub-octave-spanning bandwidths. Piecewise dispersion compensation is possible through coherent pulse synthesis schemes, but requires substantial engineering [63].

Here, we demonstrate a highly efficient adiabatic frequency downconverter that intrinsically manages its own large material dispersion (Fig. 5.1). This enables a linear transfer of amplitude and phase of near-IR pulses at Ti:sapphire wavelengths (680–820 nm) to an octave-spanning bandwidth in the mid-IR (2–4

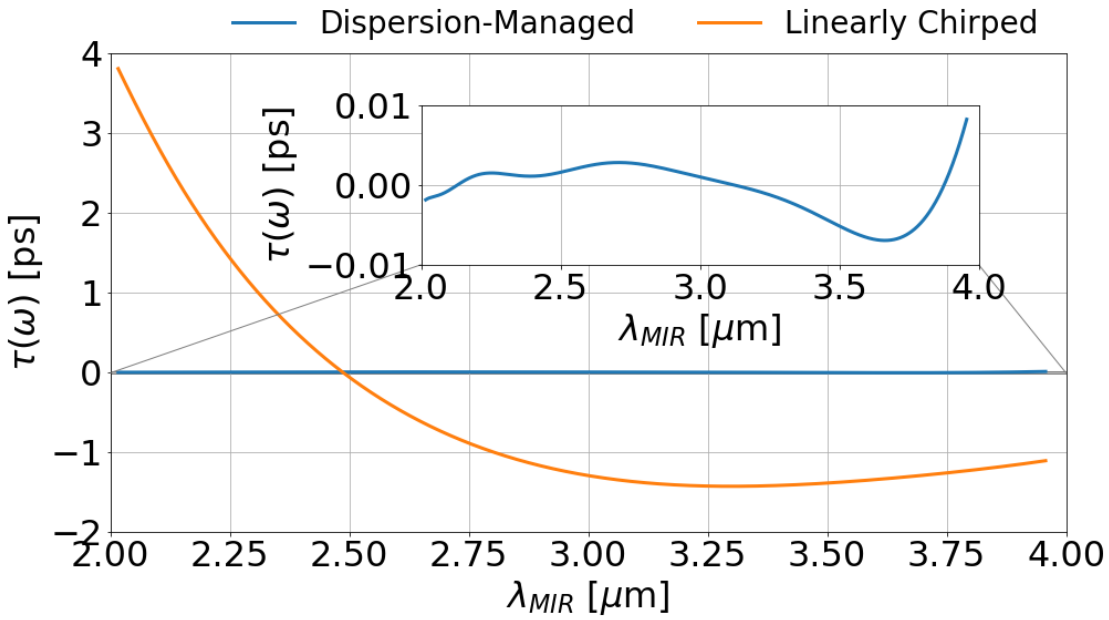

Figure 5.2: Sub-20-fs peak-to-peak residual group delay for the dispersion managed device compared to >5 ps for a device of identical conversion bandwidth and length, but with a standard, linearly chirped G(z)

μm) without the need for additional complex dispersion management. We report a 2 cm $LiNbO_3$ device that imparts only 200-300 fs^2 residual GDD over an octave-spanning bandwidth. The result is a compressed 13.5-fs near-IR pulse converted to a 15.9-fs mid-IR pulse (1.2x its transform-limited duration) with high photon conversion efficiency in the presence of a strong, narrowband pump. This constitutes a nearly complete elimination of GDD and a dramatic improvement over the > 10^4 fs^2 GDD imparted by a standard, quasi-linear QPM domain poling function, as used in [48].

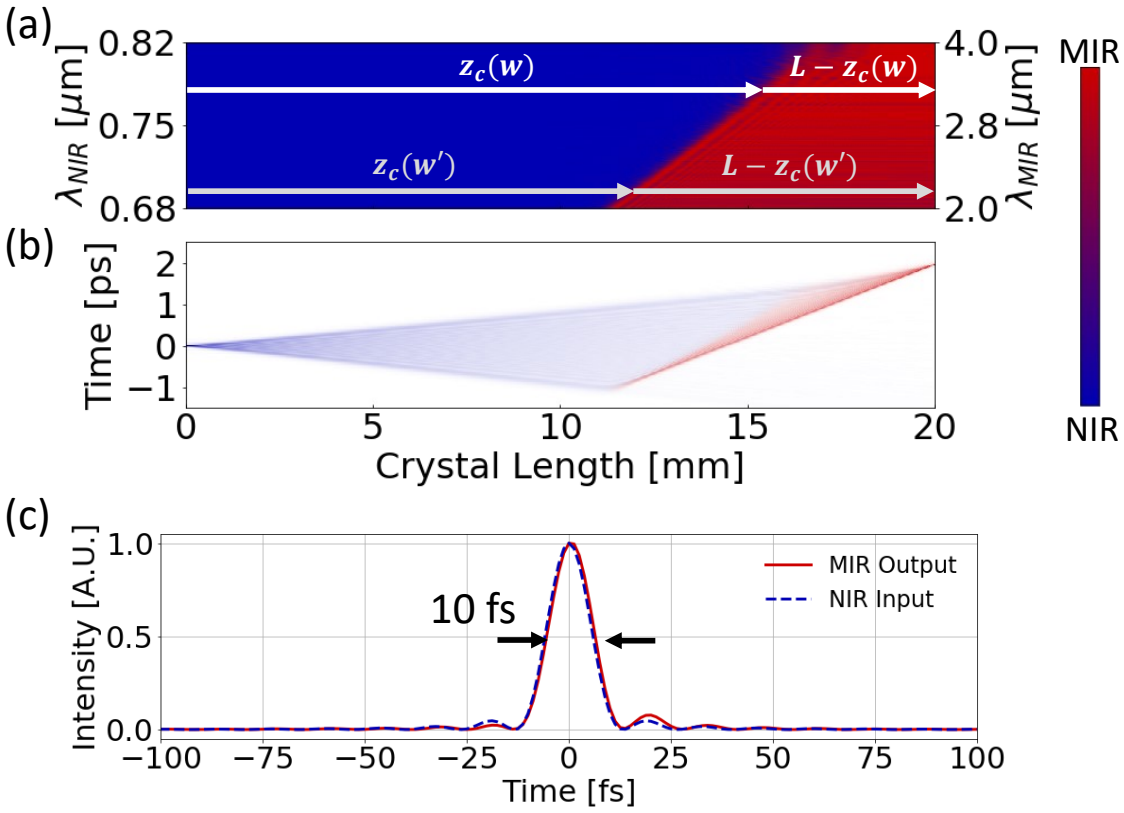

Figure 5.3: Propagation simulations of the device under study, showing (a) the position-dependent conversion of each spectral component of an input 10-fs near-IR field, (b) temporal evolution dynamics illustrating stretching of the input near-IR pulse followed by simultaneous conversion to the mid-IR and recompression to a 10-fs duration. (c) Mid-IR output pulse intensity (solid red) compared against initial compressed near-IR input pulse (dashed blue).

5.1 ADFG: BACKGROUND & DISPERSION PROPERTIES

5.1.1 ADFG Concept

Ultrafast adiabatic difference frequency generation (ADFG) is a recently established technique for efficient down-conversion of photons over a wide bandwidth [91, 65]. It is achieved using a monotonic, slowly varying position-dependent poling frequency $G(z) = 2\pi/\Lambda(z)$ to create a chirped quasi-phase

matching (QPM) device where $\Lambda(z)$ is the domain period of the structure at the propagation coordinate z. Each input frequency ω is locally converted within the device at a position $z_c(\omega)$ when the phase matching condition $\Delta k(\omega) = \Delta k_0(\omega) - G(z_c(\omega)) = 0$ where $\Delta k_0(\omega)$ is the bulk wavevector mismatch of the DFG process. Here, $\Delta k(\omega) = k_{NIR}(\omega) - k_{MIR}(\omega) - k_p$ where $k_{NIR}(\omega)$, $k_{MIR}(\omega)$, and k_p are the near-IR, mid-IR, and pump wavevectors. Note that since the pump is very narrowband, there is a one-to-one correspondence between near-IR and mid-IR frequencies. When the poling function varies slowly enough, the adiabatic condition is achieved and photons at each frequency undergo unidirectional conversion to the difference frequency field (here, the mid-IR field). The efficiency of this process has been shown to approach saturation at unity with increasing pump power [71].

ADFG has been used to produce single-cycle, energetic pulses when accompanied by a complex dispersion management scheme incorporating grism pairs and a programmable dispersive filter [48]. This work also showed the ability of ADFG to preserve complex pulse features through the conversion process. However, the device required a complicated phase mask applied by the programmable dispersive filter in order to compress the pulses. This is because of the complicated dispersion profile imparted to the downconverted pulses that is not just due to the bulk material dispersion, but also from where the light is converted within the device.

The dispersion that results from a monotonically varying aperiodic grating has been studied for both adiabatic optical parametric amplification (AOPA) [11] and ADFG [48] devices. The group delay $\tau(\omega)$ as a function of conversion

position $z_c(\omega)$ is given by:

$$\tau(\omega) = k'_{NIR}(\omega)z_c(\omega) + k'_{MIR}(\omega)(L - z_c(\omega)) \tag{5.1}$$

where the primes denote differentiation with respect to ω (see Appendix for derivation). Intuitively, this equation states that the total group delay is the sum of that acquired by the input near-IR frequency up to the conversion position plus the group delay acquired by mid-IR frequency after the conversion position. A consequence of eq. 5.1 is that the device dispersion is highly dependent on the design. A linear poling function $G(z)$ is the simplest design to maintain the adiabatic condition over a wide bandwidth, and yet it can result in a non-trivial group delay that can not be compensate for without the aid of a pulse shaper. Fig. 5.2 shows that for a linearly chirped, 2 cm, LiNbO-$_3$ device, the resulting group delay spans several picoseconds with large amounts of high order dispersion indicated by the line shape.

5.1.2 Dispersion Engineering

Here, we show how to use the frequency-dependent and localized conversion of ADFG to cancel the devices own material dispersion while generating an octave-spanning bandwidth in the mid-IR. A similar concept was described theoretically for AOPA where two devices were used in tandem to engineer a dispersion profile for the seeded field [11]. Since the desired output of and ADFG device is the unseeded field, this can be accomplished in a single device. To cancel the material dispersion of a 2 cm, $LiNbO_3$, we want to design a QPM grating such that the group delay profile is flat, i.e., $d\tau(\omega)/d\omega = 0$, to minimize group delay dispersion and higher order dispersion imparted by the device (Fig. 5.2, blue).

To design the device, we solve eq. 5.1 when $\tau(\omega) = const.$ for $z_c(\omega)$. The constant can take any value that lies between $k'_{NIR}(\omega)L$ and $k'_{MIR}(\omega)L$ for all relevant values of ω such that $z_c(\omega)$ is monotonic. The grating can then be constructed by choosing a poling period $\Lambda(z)$ such that $G(z_c(\omega)) = k_0(\omega)$ at each $z_c(\omega)$. Since $z_c(\omega)$ is continuous but the grating structure is made of discrete domains, this can be accomplished by sampling $z_c(\omega)$ according to the current position in the device after placing each domain.

Fig. 5.3a shows a simulation of the near-IR and mid-IR spectra as a function of propagation in our dispersion-managed device. The propagation-dependent conversion position of each mid-IR wavelength in the device can be seen from the sharp conversion transition. In the time domain, this results in a compressed, 10-fs near-IR input converting directly to a compressed, 10-fs mid-IR output (Fig. 5.3b,c). Conveniently, the device acts as its own stretcher/compressor, broadening an the input near-IR pulses to several picoseconds prior to conversion. This keeps the peak intensity low during conversion, then subsequently, the generated mid-IR pulses self-compressing back to a 10-fs duration (Fig. 5.3). Further $\tau(\omega)$ can be engineered to suit specific applications such as compensation of external sources of dispersion so that the input pulse itself need not be compressed.

5.2 EXPERIMENTAL RESULTS

The laser source consists of a 1030-nm Yb:YAG laser with two outputs: a 900-fs low-power (2 µJ) output and a 3-ps high-power (17 mJ) output. The 900-fs low-power output drives white-light (WL) geneartion in a 13-mm YAG crystal,

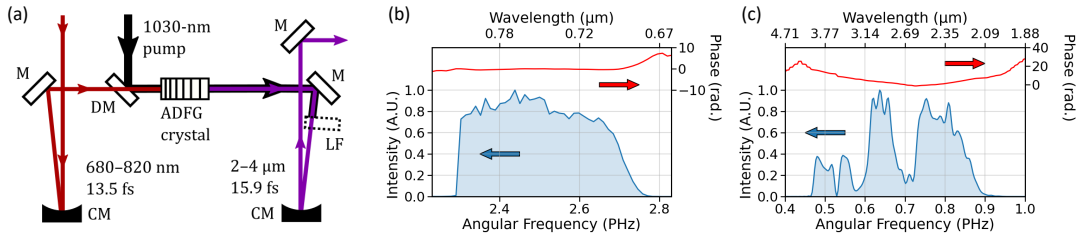

Figure 5.4: (a) ADFG experimental diagram: near-IR is focused into the ADFG crystal using a concave mirror (CM) and combined with the pump using a dichroic mirror (DM). The generated mid-IR light is collimated with a second CM. (b) NIR input spectrum and phase retrieved by FROG (c) MIR output spectrum and phase retrieved by FROSt.

from which, a bandwidth of 670–950 nm is selected and amplified to 50 µJ in a series of noncollinear optical parametric chirped pulse amplifiers pumped with frequency-doubled light from the high-power output. The amplified near-IR pulse is split into several paths. The first is sent to the adiabatic frequency converter to generate the 2–4 µm mid-IR pulse. A 4f fourier-domain pulse shaper (PhaseTech, Inc.) is used to spectrally filter the near-IR pulse to 680–820 nm and compress it at the input of the adiabatic frequency conversion stage. A second near-IR beam, compressed with a chirped mirror pair, is used as the pump pulse for frequency-resolved optical switching (FROSt), described below, which is used to characterize the generated mid-IR pulse.

5.2.1 ADFG experimental setup

The ADFG setup is shown in Figure 5.4a. The compressed 680–820-nm near-IR pulse is combined with 200 µJ of 1030-nm pump light in the ADFG crystal generating a compressed 2–4-µm mid-IR pulse. The near-IR beam is focused into the frequency conversion crystal with a 50-cm concave mirror and combined

with the pump pulse using a shortpass dichroic mirror. A longpass filter (Andover 1750-nm longpass filter, 1-mm Si) is used to separate the mid-IR pulse from the residual near-IR and pump light. The mid-IR light is collimated using a 50-cm concave mirror.

The near-IR pulse is characterized after the dichroic mirror by bypassing the ADFG stage and using SHG FROG. Using the 4f pulse shaper, we impart a phase to the near-IR pulses so they are compressed at the input to the ADFG device. The measured spectrum and retrieved phase is shown in Fig. 5.4b.

We achieve a nearly flat 70% photon conversion efficiency across the input near-IR spectrum. The generated mid-IR spectrum is shown in Fig. 5.4c. A number of modulations are observed across the mid-IR and have been identified with a parasatic OPA process that occur at the end of the device in a region that is non-critical to the dispersion properties of the device.

5.2.2 FROSt Measurement

We characterize our octave-spanning mid-IR pulses using frequency resolved optical switching (FROSt). FROSt is a phase-matching-free characterization technique that was recently used to characterize two-octave-spanning infrared pulses [54, 59]. In FROSt, a pump pulse is used to excite free-carriers in a semiconductor sample creating a sharp absorption edge in time which acts as an optical gate for characterizing a probe pulse. The probe pulse spectrum is measured as a function of pump-probe delay, allowing the electric field of the probe pulse to be reconstructed using a ptychographic algorithm [54].

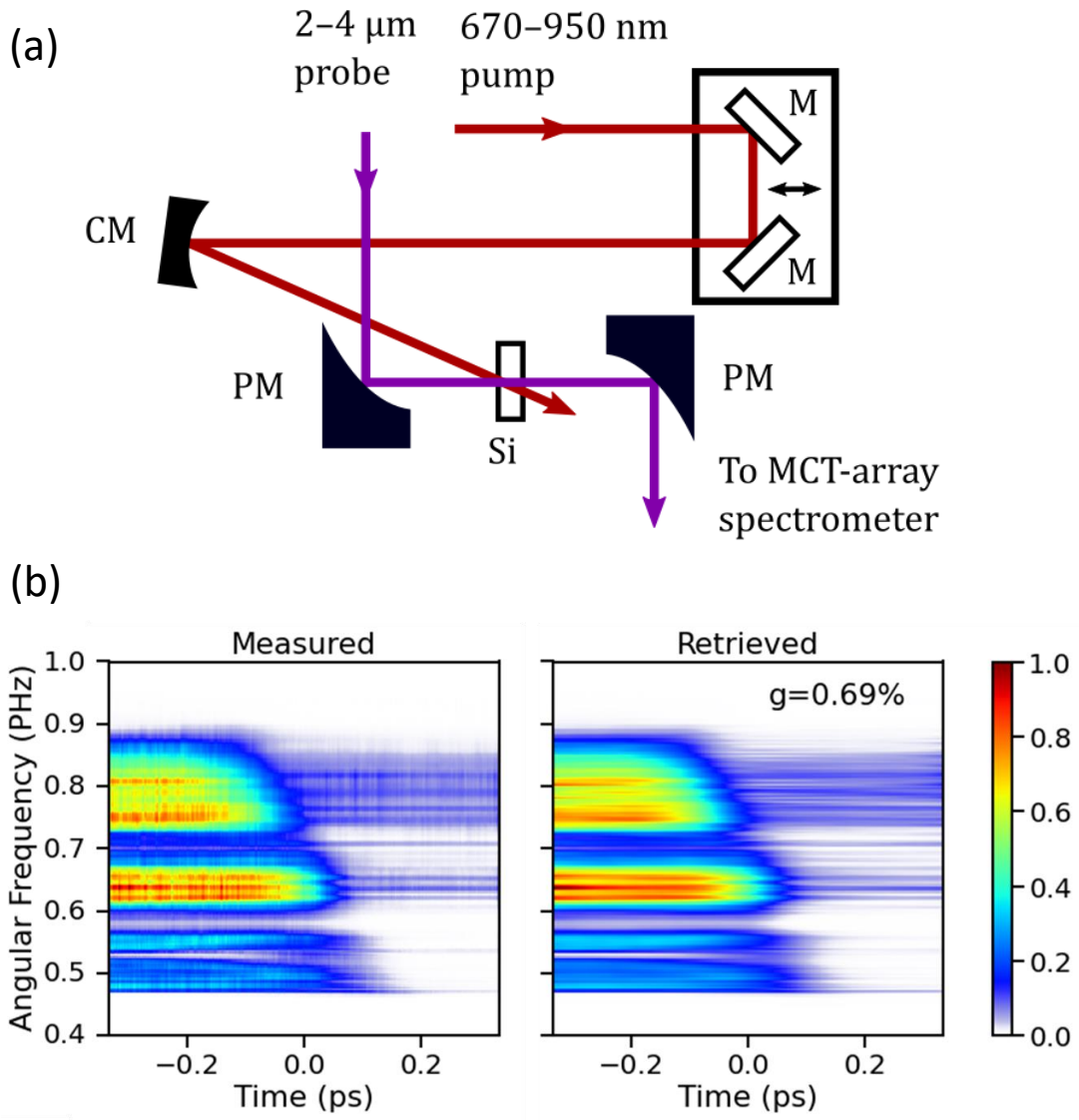

Figure 5.5: (a) FROSt setup: the mid-IR probe is focused onto the Si sample using an off-axis parabolic mirror (PM) and recollimated with a second PM. The near-IR delay is scanned with an automated delay stage and focused onto the sample with a concave mirror (CM). (b) Measured and retrieved FROSt traces

We use a 10-μJ near-IR pulse compressed to 14-fs FWHM to pump the free-carrier excitation in a 1-mm Si sample. The pump and probe pulses are combined at the FROSt sample as shown in Fig. 5.5a. The probe is focused to a 44-μm $1/e^2$ beam diameter at the sample. To achieve a strong, uniform free-carrier excitation across the probe beam, the pump is focused to a 275-μm $1/e^2$ beam diameter. The measured and retrieved FROSt trace for the probe is shown in Fig. 5.5b. The retrieval gives a reconstruction of the mid-IR electric field profile and phase.

The group delay imparted by the device can now be determined by comparing the near-IR spectral phase measured with SHG FROG and the output mid-IR spectral phase measured with FROSt. The spectral phase imparted by our device ϕ_D and related group delay $\tau(\omega) = (d\phi_D(\omega))/d\omega$ is calculated by $\phi_D = \phi_{MIR} - \phi_{NIR} - \phi_{Optics}$, where $\phi_{MIR}(\phi_{NIR})$ is the measured spectral phase of the mid-IR (near-IR) pulse and ϕ_{Optics} is the analytic spectral phase of a 1-mm fused silica beamsplitter in the SHG FROG setup calculated from the Sellmeier equation and the measured spectral phase of a 1-mm silicon longpass filter.

5.2.3 Results

The GD imparted by our device is shown in Fig. 5.6a. The maximum range of group delay is 250 fs over the target bandwidth (2–4 μm) resulting in a 15.9-fs pulse with a small satellite (5.6b, orange). The output MIR pulse is 1.2x the 13.5-fs input pulse duration without external dispersion compensation. The small residual GDD is estimated by applying a linear fit across the target bandwidth, indicating -210 fs^2 (Fig. 5.6a, dashed). This dispersion may have arisen due to

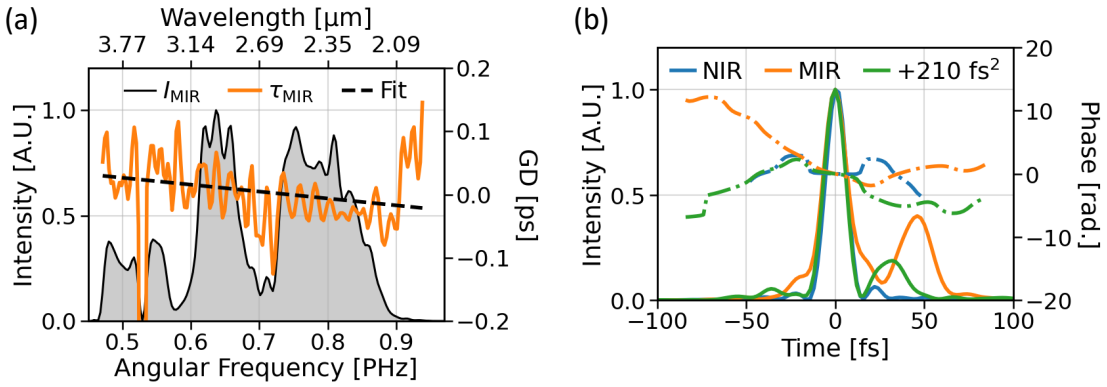

Figure 5.6: (a) Measured MIR spectrum (filled curve) and group delay imparted by the device (orange) with a linear fit (black). (b) Retrieved pulse intensities (solid) and phase (dashed-dotted) of the near-IR input (blue), mid-IR (orange), and residual-GDD-compensated mid-IR (green).

manufacturing tolerances in the device and could potentially be compensated via a thin wedge pair or slightly modified design. When this residual GDD is compensated, the output pulse duration is reduced to 14 fs (Fig. 5.6b, green), 1.04x the input pulse duration.

5.3 DISCUSSION

In summary, we have demonstrated the proof-of-principle of a concept for generating single-cycle mid-IR pulses efficiently by adiabatic down-conversion of a few-cycle near-IR source, in a monolithic device imparting near-zero GDD. Alternatively, the device could be designed to impart a desired dispersion profile in combination with a small amount of bulk material dispersion. This would enable high energy frequency conversion by avoiding high peak intensities in the device.

We believe this work is an important step in advancing the state of the art

for ultrafast lasers and the study ultrafast science. By compensating for its own dispersion and/or the dispersion of other components of the laser architecture, the dispersion managed ADFG concept can greatly reduce the complexity, cost, and time investment of building ultrafast laser systems. It also serves to enhance the modularity and compactness of ultrafast frequency conversion stages by eliminating the need for the sophisticated dispersion compensation stages. Such stages introduce instability by increasing extra beam paths and optics and have to be tailored to the specific conversion device, making them inflexible.

[1]

[1]This chapter contains material from [29, 36].

CHAPTER 6

CONCLUSION

To summarize the results of this dissertation, we have analyzed the evolution dynamics of hybridized OPA and idler SHG – which we call second harmonic amplification (SHA) – and found it suited to overcome one of the major problems limiting the conversion efficiency of parametric amplifiers: the spatiotemporally inhomogeneous conversion that is a result of the intensity-dependent conversion-back-conversion cycles. Chapter 2 revealed that the dynamics of SHA are those of a damped anharmonic oscillator, describable by a Duffing oscillator model. This model also describes the dynamics of conventional OPA and OPA with linear idler loss (as due to absorption). Our analysis thus unifies the description of OPA and its variants that incorporate the displacement of idler photons – including the recently demonstrated QPA approach [60, 61] – and may be useful for the analysis and design of many parametric amplifier systems.

Further, Chapter 2 explored two device examples investigated by a numerical analysis that indicates a high expected pump-to-signal energy conversion efficiency (as high as 55% in one example) in common bulk nonlinear media used for OPA. These results hold for the Gaussian pump beam and pulse profiles commonly obtained from pump lasers. Our examples included devices pumped by picosecond lasers at 1-μm and 2-μm wavelength that produce amplified signal pulses and accompanying idler SH pulses with picosecond and < 200-fs TL duration.

In Chapter 3, we experimentally demonstrated SHA, validating the predictions that the introduction of idler SHG could suppress back-conversion to ob-

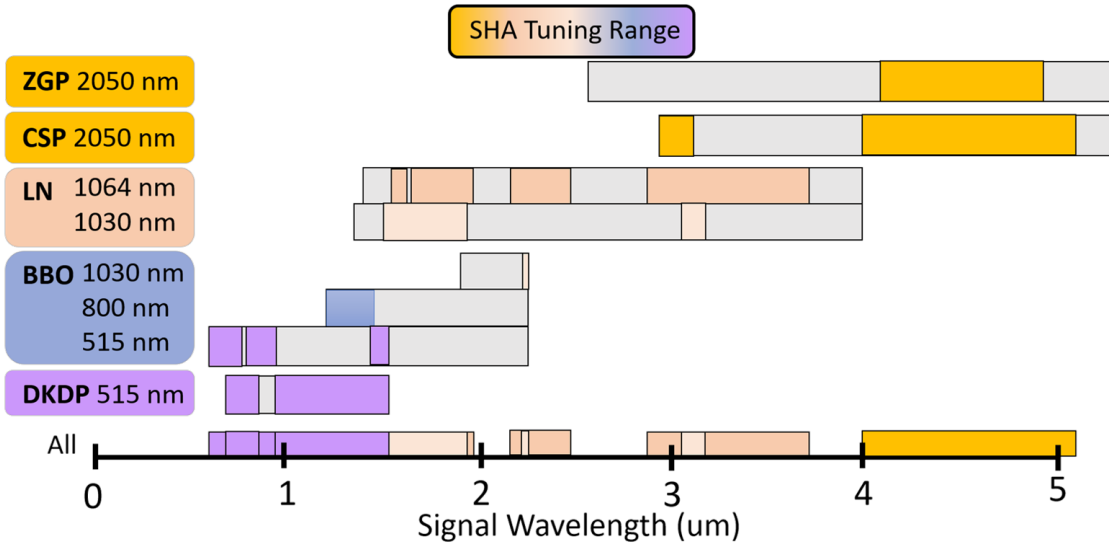

Figure 6.1: Tuning range of non-collinear SHA showing that phase matching is possible for efficiently generating a wide range wavelengths using common pump lasers and nonlinear media [18].

tain highly efficient OPA. 44% pump to signal energy conversion was achieved corresponding to 68% pump depletion, a several fold increase in efficiency over conventional OPA. We verified that the signal maintains a high quality beam shape throughout the conversion and from the idler SH beam measurements, we deduced that the primary limitation on efficiency is due to spatial walk-off of the idler SH beam. This could be mitigated by using larger beam sizes. Additionally, the pump beam evolution depicts the first clear evidence of the damped oscillatory nature of the SHA interaction.

Having now demonstrated that SHG works to enhance OPA efficiency as predicted, there are a number of promising avenues to be explored that take advantage of SHAs fully parametric nature. First, there are many degrees of freedom that can be leveraged to achieve simultaneous phase matching of OPA and SHG. Prior investigations have shown this to be possible over a wide range of existing nonlinear media (such as BBO, CSP, and $LiNbO_3$) using non-collinear

geometries [18] and quais-phase matching (QPM) [31]. Non-collinearity can provide a wide frequency tuning range in a single crystal and is a route toward tunable and efficient downconversion of high average power 1- and 2-μm solid-state diode-pumped lasers due to the large aperture of available bulk nonlinear media 6.1. QPM can enable arbitrary phase matching within the transparency range of materials such as $LiNbO_3$, KTP, and GaAs provided manufacturing constraints and energy conservation between frequencies are observed. A further advantage of QPM is the ability to tune the relative nonlinear strength of OPA and SHG through the poling structure in order to tune the damping parameter toward the critical damping regime. This could enable rapid conversion by operating near the critical damping point to avoid the oscillatory dynamics of the underdamped regime.

A unique advantage of using a nonlinear parametric process to induce efficient OPA in place of loss is that the lost idler energy is preserved in the copropagating idler SH field. On account of SHA's high photon conversion efficiency, one might envision using cascaded SHA stages to obtain a pump-to-signal energy conversion efficiency that reaches or even exceeds the OPA quantum defect limit (i.e., an efficiency $\geq \omega_s/\omega_p$), as the substantial power in the idler SH field could be reused in a second SHA stage to further amplify the signal. This scheme, depicted in Fig. 6.2, works if $\omega_{2i} > \omega_s$ (equivalent to $\omega_s < (2/3)\omega_p$). Defining η_i as the pump photon depletion efficiency for the i^{th} stage (and assuming there are no residual idler photons), the overall energy conversion efficiency of pump to signal in this scheme is $(\eta_1^2 + \eta_1\eta_2/2)(\omega_s/\omega_p)$. Thus, for example, it is possible for the pump-to-signal energy conversion efficiency to equal the quantum defect limited efficiency for a per-stage photon conversion efficiency $\eta_1 = \eta_2 = 81.6\%$. A maximum energy conversion efficiency at 150% above the

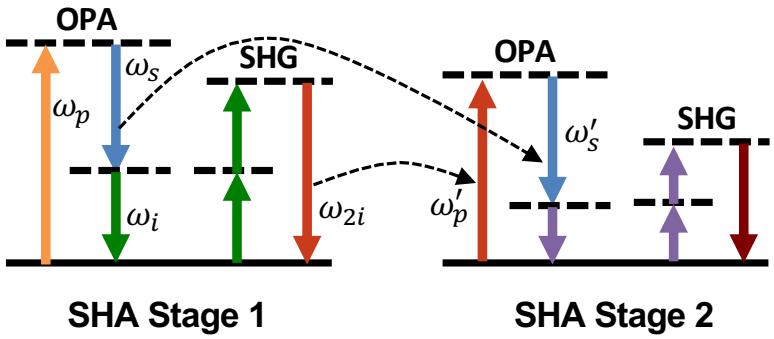

Figure 6.2: Cascaded SHA stage scheme potentially capable of exceeding the quantum-limited OPA efficiency, ω_s/ω_p, for a high enough single-stage photon conversion efficiency. The idler SH from the first stage is reused to amplify the signal in the second stage, such that $\omega_p^{'} = \omega_{2i}$ and $\omega_s^{'} = \omega_s$. Each stage would incorporate an appropriate material and phase-matching scheme for SHA.

quantum defect is theoretically possible for $\eta_1 = \eta_2 = 100\%$. In the example of Section 2.2.1, the pump photon depletion efficiency is 80% and only 3% of the incident pump energy is lost to the idler wave, and is thus close to but not quite at the efficiency threshold needed for exceeding the quantum limit if repeated in an equally efficient subsequent stage where the idler SH is resused to pump the signal. This scheme therefore presents an intriguing future direction for achieving ultra-efficient parametric amplification, and may be especially useful for mid-wave and long-wave mid-infrared amplifiers pumped by near-infrared lasers, which possess a low quantum defect and are therefore very inefficient.

In chapter 4, the concept of using SHG as a loss channel to tailor dynamics was extended to TWM using analyses techniques typical of non-Hermitian physics. We showed that the evolution behavior of a Hermitian wave-mixing system is tied to the non-Hermitian behavior of an enclosed subsystem, even through a full nonlinear power exchange. This behavior can be achieved because of the absence of any real loss or coupling to a thermal bath. Inducing this behavior by coherent coupling to a co-propagating wave can circumvent

other problems. As pointed out previously, thermal loading can be avoided [31] and phase noise improved [81, 82], and the loss band can be chosen by phase-matching technique rather than being tied to material or structural resonances. More generally, the use of non-Hermitian physics to explicitly control an enclosing Hermitian system, as shown here, may have broader applicability outside of optics.

Clearly, using SHG as a form of nonlinear loss can lead to a vast range of applications. In addition to added flexibility of using a phase-matchable loss mechanism in place of a material or structural resonance, the ability to preserve the lost energy in a copropagating field is of particular importance where energy efficiency and sustainability are of concern.

In chapter 5, we focused on another issue that arises due to conversion cycles, the efficiency-bandwidth trade-off. We demonstrated a proof-of-principle concept for generating single-cycle mid-IR pulses efficiently by adiabatic down-conversion of a few-cycle near-IR source in a monolithic device imparting near-zero group delay across and octave-spanning bandwidth. This solves the problem of the complex dispersion imparted by the frequency dependent conversion position in ADFG devices. By compensating for its own dispersion and/or the dispersion of other components of the laser architecture, the dispersion managed ADFG concept can greatly reduce the complexity, cost, and time investment of building ultrafast laser systems. It also serves to enhance the modularity and compactness of ultrafast frequency conversion stages by eliminating the need for the sophisticated dispersion compensation stages. Such stages introduce instability by increasing extra beam paths and optics and have to be tailored to the specific conversion device, making them inflexible. We believe

this is an important step in advancing the state of the art for ultrafast lasers and the study of ultrafast science.

[1]

[1]This chapter uses material from [31, 30]

APPENDIX A

EVALUATION OF DIFFRACTION AND BEAM WALK-OFF IN SHA

We performed an initial analysis of beam propagation effects in order to find the smallest beam size where diffraction and Poynting vector walk-off are negligible for the SHA device considered in our study. Monochromatic fields at frequencies $\omega_{j,0}$ for signal, pump, idler, and idler SH waves with 1D spatial Gaussian beam profiles were propagated in the plane of Poynting vector walk-off (spatial coordinate x) using the four coupled pulse propagation equations for OPA and idler SHG (shown in the spatial Fourier domain) with diffraction and Poynting vector walk-off:

$$d_z E_s(k_x) = i\frac{\omega_{s,0} d_{\text{eff}}}{n_s c}\mathcal{F}\{E_p(x)E_i^*(x)\} - ik_s(\omega_{s,0})E_s(k_x) + i\frac{k_x^2}{2k_s(\omega_{s,0})}E_s(k_x) \tag{A.1a}$$

$$d_z E_p(k_x) = i\frac{\omega_{p,0} d_{\text{eff}}}{n_p c}\mathcal{F}\{E_s(x)E_i(x)\} - ik_p(\omega_{p,0})E_p(k_x) + i\rho_p k_x E_p(k_x) + i\frac{k_x^2}{2k_p(\omega_{p,0})}E_p(k_x) \tag{A.1b}$$

$$d_z E_i(k_x) = i\frac{\omega_{i,0} d_{\text{eff}}}{n_i c}\mathcal{F}\left\{E_p(x)E_s^*(x) + E_{2i}(x)E_i^*(x)\right\} - ik_i(\omega_{i,0})E_i(k_x) + i\frac{k_x^2}{2k_i(\omega_{i,0})}E_i(k_x) \tag{A.1c}$$

$$d_z E_{2i}(k_x) = i\frac{\omega_{2i,0} d_{\text{eff}}}{2n_{2i} c}\mathcal{F}\{E_i^2(x)\} - ik_{2i}(\omega_{2i,0})E_{2i}(k_x) + i\rho_{2i}k_x E_{2i}(k_x) + i\frac{k_x^2}{2k_{2i}(\omega_{2i,0})}E_{2i}(k_x) \tag{A.1d}$$

where $E_j(k_x) = A_j(k_x)e^{ik_j(\omega_{j,0})z}$, and A_j, k_j, and n_j are the signal, pump, idler, and idler SH electric field amplitudes, wave vectors in the nonlinear medium, and indices of refraction, respectively, and where k_x and z are the transverse spatial and propagation coordinates. The effective quadratic nonlinear coefficient is given by d_{eff} and c is the speed of light. Terms quadratic in k_x represent diffraction in the paraxial regime. Terms linear in k_x represent Poynting vector walk-

off, which in CSP is present for pump and idler SH but not signal and idler, as both OPA and SHG processes are Type-I ($o + o = e$). The walk-off angles for the pump and idler SH are given by ρ_p and ρ_{2i}, respectively.

Fig. A.1 shows the results for the CSP device simulated in Section 2.2.1, where both diffraction and spatial walk-off are of concern. ρ_p and ρ_{2i} for the 1.03 μm pump and 3.25 μm idler SH in this case are 16.64 μrad and 16.82 μrad, respectively. For the 2.55 mm optimal crystal length used in the simulation, this corresponds to ~40 μm of walk-off for the pump. Fig. A.1 shows the spatial simulation results of solving Eqs. (S1)-(S4) for three beam sizes, $1/e^2$ beam radii 1, 0.5, and 0.2 mm. For a 1 mm beam radius (the pump beam radius used in the CSP device example in the main text), we find negligible contribution from diffraction and walk-off, resulting in dynamics identical to the simulations where these effects are not included (top two panels). Decreasing to a 0.5 mm beam radius, a very slight deviation appears in the last 10% of the crystal length, with minor back-conversion setting in just as the crystal terminates. Decreasing even further to a 0.2 mm beam radius, there is no longer a region within the crystal where conversion cycles are fully damped out. These results show that ignoring spatial effects is an excellent approximation for a 1.0 mm pump beam radius and marginal at a 0.5 mm beam radius. At 0.2 mm radius, diffraction and spatial walk-off have a strong effect on the evolution by inducing mixing between fields at different spatial coordinates that disturbs the local dynamics of SHA.

This analysis illustrates that spatial effects can disturb the SHA dynamics, preventing uniform spatiotemporal amplification. However, the use of suitably large beams circumvents the problem.

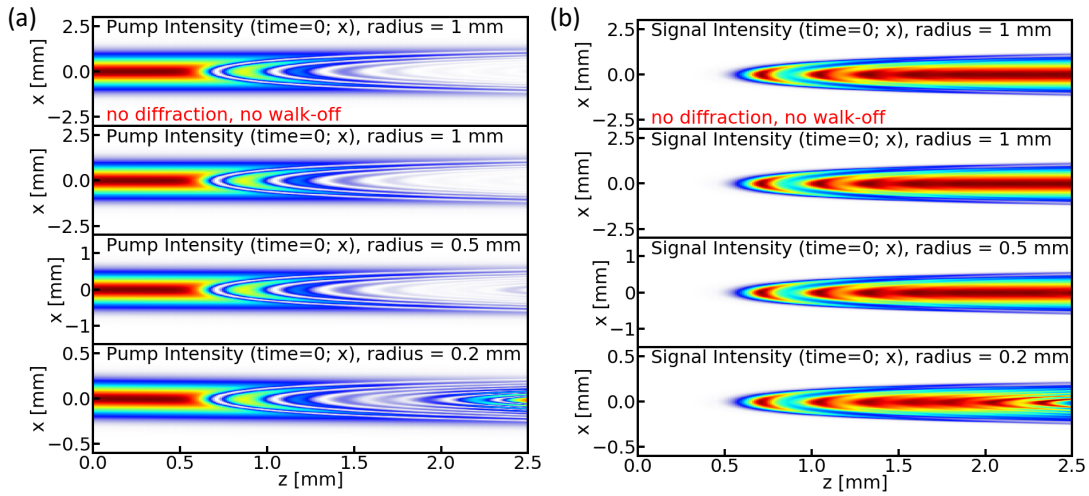

Figure A.1: Spatial beam propagation dynamics for Type-I (*ooe*) phase-matched OPA and idler SHG in CSP at time = 0 for (a) pump beams of radius 1, 0.5, and 0.2 mm ($1/e^2$) and (b) the corresponding signal. The first panels of (a) and (b) show the 1 mm beam radius case where all spatial propagation effects are neglected from the simulation. Simulation parameters correspond to the device parameters in Section 2.2.1.

APPENDIX B

NUMERICAL MODEL FOR FULL SPATIOTEMPORAL PROPAGATION ANALYSIS

For the CSP and LNB devices simulated in the main text, diffraction and spatial walk-off were found to have negligible effect as a result of the large beam size. Thus full spatiotemporal evolution (two transverse spatial dimensions plus one temporal dimension) along the propagation axis could be solved without spatial derivative terms. Each coordinate of a radially symmetric transverse spatial axis (r) was calculated independently with a temporal grid to capture temporal propagation effects. Using a Fourier split-step method, we solved the following four coupled pulse propagation equations for OPA and idler SHG (shown in the frequency domain), accounting for the exact frequency-dependent dispersion, $k_j(\omega)$, given by published Sellmeier equations:

$$d_z E_s(\omega, r) = i\frac{\omega_{s,0} d_{\text{eff}}}{n_s c}\mathcal{F}\{E_p(t,r)E_i^*(t,r)\} - ik_s(\omega)E_s(\omega,r) \tag{B.1a}$$

$$d_z E_p(\omega, r) = i\frac{\omega_{p,0} d_{\text{eff}}}{n_p c}\mathcal{F}\{E_s(t,r)E_i(t,r)\} - ik_p(\omega)E_p(\omega,r) \tag{B.1b}$$

$$d_z E_i(\omega, r) = i\frac{\omega_{i,0} d_{\text{eff}}}{n_i c}\mathcal{F}\left\{E_p(t,r)E_s^*(t,r) + E_{2i}(t,r)E_i^*(t,r)\right\} - ik_i(\omega)E_i(\omega,r) \tag{B.1c}$$

$$d_z E_{2i}(\omega, r) = i\frac{\omega_{2i,0} d_{\text{eff}}}{2n_{2i} c}\mathcal{F}\{E_i^2(t,r)\} - ik_{2i}(\omega)E_{2i}(\omega,r) \tag{B.1d}$$

where $E_j(\omega, r) = A_j(\omega, r)e^{ik_j(\omega_{j,0})z}$. The power and power spectrum can then be computed by integration over space $P(t) = 4\pi c\epsilon_0 \int_0^\infty |E_j(t,r)|^2 r dr$ and $S(\omega) = 4\pi c\epsilon_0 \int_0^\infty |E_j(\omega,r)|^2 r dr$, respectively. Integrating either of these over time yields the total energy. This model allowed us to capture all non-negligible propagation effects consistent with a collinear geometry. Nonlinear polarization terms beyond quadratic order were not included.

APPENDIX C

DERIVATION OF ADFG GROUP DELAY

Consider difference frequency mixing between an input field at ω and a strong pump field at ω_p in an aperiodically poled crystal described by the z-dependent wavenumber $G(z)$ where $\omega_p < \omega$. In the limit of instantaneous conversion, the phase of the difference frequency field at $\omega - \omega_p$ is the sum of two terms: first is the contribution from the input waves and grating up to the conversion point and second is the linear propagation of the difference frequency field after the conversion point. The first term is given by the phase matching condition at the conversion point, $z_c(\omega)$:

$$\phi_1(\omega - \omega_p; z_c(\omega)) = \phi(\omega; z_c(\omega)) - \phi(\omega_p; z_c(\omega)) - \phi_G(z_c(\omega))$$

Note that the pump and grating phase can be ignored for bulk or periodically poled media, but are frequency-dependent for aperiodically poled media due to the localized conversion position and will thus contribute to the group delay. Writing the phase explicitly in terms of wavevectors:

$$\begin{aligned}\phi_1(\omega - \omega_p; z_c(\omega)) &= \int_0^{z_c(\omega)} k(\omega) - k(\omega_p) - G(z)dz \\ &= k(\omega)z_c(\omega) - k(\omega_p)z_c(\omega) - \int_0^{z_c(\omega)} G(z)dz \\ &= k(\omega)z_c(\omega) - k(\omega_p)z_c(\omega) - \int_{\omega_0}^{\omega} G(z_c(\omega'))\frac{dz_c(\omega')}{d\omega'}d\omega'.\end{aligned}$$

For the third term, I've used the definition of line-integrals to change the integration of the grating wavevector to be over ω. This assumes $z_c(\omega)$ is bijectively parameterized on $[\omega_0, \omega]$ and $z_c(\omega_0) = 0$ (i.e. this won't work beyond any turning points in the conversion position without piecewise parameterization). Importantly, we should recognize $G(z_c(\omega)) = \Delta k_0(\omega) = k(\omega) - k(\omega_p) - k(\omega - \omega_p)$ is the phase mismatch of a bulk device for difference frequency mixing between ω and ω_p. The phase of the difference frequency field at the point of conversion can then be written:

$$\phi_1(\omega - \omega_p; z_c(\omega)) = k(\omega)z_c(\omega) - k(\omega_p)z_c(\omega) - \int_{\omega_0}^{\omega} \Delta k_0(\omega') \frac{dz_c(\omega')}{d\omega'} d\omega'.$$

The second phase term for a device of length L is simply $\phi_2(\omega - \omega_p; L - z_c(\omega)) = k(\omega - \omega_p)(L - z_c(\omega))$. Thus, the total phase is:

$$\begin{aligned}
\phi(\omega - \omega_p; L) =& \phi_1(\omega - \omega_p; z_c(\omega)) + \phi_2(\omega - \omega_p; z_c(\omega)) \\
=& k(\omega)z_c(\omega) - k(\omega_p)z_c(\omega) - \int_{\omega_0}^{\omega} \Delta k_0(\omega') \frac{dz_c(\omega')}{d\omega'} d\omega' + k(\omega - \omega_p)(L - z_c(\omega)) \\
=& [\Delta k_0(\omega)z_c(\omega)]_{\omega_0}^{\omega} - \int_{\omega_0}^{\omega} \Delta k_0(\omega') \frac{dz_c(\omega')}{d\omega'} d\omega' + k(\omega - \omega_p)L \\
=& \int_{\omega_0}^{\omega} \frac{d\Delta k_0(\omega')}{d\omega'} z_c(\omega') d\omega' + k(\omega - \omega_p)L
\end{aligned}$$

where I've used integration by parts to simplify the expression. The group delay is now easy to calculate:

$$\begin{aligned}\tau(\omega-\omega_p,L) =& \frac{d\phi(\omega-\omega_p;L)}{d\omega}\\ =& \frac{d\Delta k_0(\omega)}{d\omega}z_c(\omega)+\frac{dk(\omega-\omega_p)}{d\omega}L\\ =& \frac{dk(\omega)}{d\omega}z_c(\omega)+\frac{dk(\omega-\omega_p)}{d\omega}(L-z_c(\omega))\end{aligned}$$

which is the intended result.

BIBLIOGRAPHY

[1] S. A. Akhmanov and R. V. Khokhlov. Concerning one possibility of amplification of light waves. *Sov. Phys. JETP*, 16:252–257, 1963.

[2] J. A. Armstrong, N. Bloembergen, J. Ducuing, and P. S. Pershan. Interactions between light waves in a nonlinear dielectric. *Phys. Rev.*, 127:1918–1939, Sep 1962.

[3] O. Aytur and Y. Dikmelik. Plane-wave theory of self-doubling optical parametric oscillators. *IEEE J. Quantum Electron.*, 34(3):447–458, 1998.

[4] V. Bagnoud, I. Begishev, M. Guardalben, J. Puth, and J. Zuegel. 5 hz, ¿ 250 mj optical parametric chirped-pulse amplifier at 1053 nm. *Opt. Lett.*, 30:1843–1845, 2005.

[5] Eyal Bahar, Xiaoyue Ding, Asaf Dahan, Haim Suchowski, and Jeffrey Moses. Adiabatic four-wave mixing frequency conversion. *Opt. Express*, 26(20):25582–25601, 2018.

[6] I A Begishev, A A Gulamov, E A Erofeev, É A Ibragimov, Sh R Kamalov, T Usmanov, and A D Khadzhaev. Highly efficient parametric amplification of optical beams. i. optimization of the profiles of interacting waves in parametric amplification. *Sov. J. Quantum Electron.*, 20(9):1100–1103, sep 1990.

[7] Arik Bergman, Robert Duggan, Kavita Sharma, Moshe Tur, Avi Zadok, and Andrea Alù. Observation of anti-parity-time-symmetry, phase transitions and exceptional points in an optical fibre. *Nat. Commun.*, 12(486):1–9, Jan 2021.

[8] Huseyin Cankaya, Anne-Laure Calendron, Haim Suchowski, and Franz X. Kärtner. Adiabatic sum-frequency generation in the visible region. In *Advanced Solid-State Lasers Congress*, page ATu4A.9. Optical Society of America, 2013.

[9] H. Cao, S. Tóth, M. Kalashnikov, V. Chvykov, and K. Osvay. Highly efficient, cascaded extraction optical parametric amplifier. *Opt Express*, 26:7516–7527, 2018.

[10] Giulio Cerullo and Sandro De Silvestri. Ultrafast optical parametric amplifiers. *Rev. Sci. Instrum.*, 74(1):1–18, 2003.

[11] M. Charbonneau-Lefort, M. M. Fejer, and Bedros Afeyan. Tandem chirped quasi-phase-matching grating optical parametric amplifier design for simultaneous group delay and gain control. *Opt. Lett.*, 30(6):634–636, Mar 2005.

[12] Mathieu Charbonneau-Lefort, Bedros Afeyan, and M. M. Fejer. Optical parametric amplifiers using chirped quasi-phase-matching gratings i: practical design formulas. *J. Opt. Soc. Am. B*, 25(4):463–480, Apr 2008.

[13] Bo-Han Chen, Emanuel Wittmann, Yuya Morimoto, Peter Baum, and Eberhard Riedle. Octave-spanning single-cycle middle-infrared generation through optical parametric amplification in ligas2. *Opt. Express*, 27(15):21306–21318, Jul 2019.

[14] Chong Chen, Liang Jin, and Ren-Bao Liu. Sensitivity of parameter estimation near the exceptional point of a non-Hermitian system. *New J. Phys.*, 21(8):083002, Aug 2019.

[15] Weijian Chen, Şahin Kaya Özdemir, Guangming Zhao, Jan Wiersig, and Lan Yang. Exceptional points enhance sensing in an optical microcavity. *Nature*, 548(7666):192–196, Aug 2017.

[16] M. H. Chou, K. R. Parameswaran, M. M. Fejer, and I. Brener. Multiple-channel wavelength conversion by use of engineered quasi-phase-matching structures in linbo3 waveguides. *Opt. Lett.*, 24(16):1157–1159, Aug 1999.

[17] P. B. Corkum and Ferenc Krausz. Attosecond science. *Nat. Phys.*, 3(6):381–387, June 2007.

[18] Devin J. Dean, Noah Flemens, Dylan Heberle, and Jeffrey Moses. Widely tunable second harmonic amplification by noncollinear phase matching in bulk birefringent materials. In *Nonlinear Frequency Generation and Conversion: Materials and Devices XX*, volume 11670, pages 70–78. SPIE, Apr 2021.

[19] Xiaoyue Ding, Dylan Heberle, Kerrianne Harrington, Noah Flemens, Wei-Zung Chang, Tim A. Birks, and Jeffrey Moses. Observation of rapid adiabatic passage in optical four-wave mixing. *Phys. Rev. Lett.*, 124:153902, Apr 2020.

[20] Jörg Doppler, Alexei A. Mailybaev, Julian Böhm, Ulrich Kuhl, Adrian Girschik, Florian Libisch, Thomas J. Milburn, Peter Rabl, Nimrod Moi-

seyev, and Stefan Rotter. Dynamically encircling an exceptional point for asymmetric mode switching. *Nature*, 537(7618):76–79, Sep 2016.

[21] A. Dubietis, R. Butkus, and A. P. Piskarskas. Trends in chirped pulse optical parametric amplification. *IEEE J. Sel. Top. Quantum Electron.*, 12(2):163–172, 2006.

[22] Charles G. Durfee, Lino Misoguti, Sterling Backus, Henry C. Kapteyn, and Margaret M. Murnane. Phase matching in cascaded third-order processes. *J. Opt. Soc. Am. B*, 19(4):822–831, Apr 2002.

[23] R. El-Ganainy, J. I. Dadap, and R. M. Osgood. Optical parametric amplification via non-hermitian phase matching. *Opt. Lett.*, 40(21):5086–5089, Nov 2015.

[24] Ramy El-Ganainy, Mercedeh Khajavikhan, Demetrios N. Christodoulides, and Sahin K. Ozdemir. The dawn of non-Hermitian optics. *Commun. Phys.*, 2(37):1–5, Mar 2019.

[25] Ramy El-Ganainy, Konstantinos G. Makris, Mercedeh Khajavikhan, Ziad H. Musslimani, Stefan Rotter, and Demetrios N. Christodoulides. Non-hermitian physics and pt symmetry. *Nat. Phys.*, 14(1):11–19, Jan 2018.

[26] Hanieh Fattahi, Helena G. Barros, Martin Gorjan, Thomas Nubbemeyer, Bidoor Alsaif, Catherine Y. Teisset, Marcel Schultze, Stephan Prinz, Matthias Haefner, Moritz Ueffing, Ayman Alismail, Lénárd Vámos, Alexander Schwarz, Oleg Pronin, Jonathan Brons, Xiao Tao Geng, Gunnar Arisholm, Marcelo Ciappina, Vladislav S. Yakovlev, Dong-Eon Kim, Abdallah M. Azzeer, Nicholas Karpowicz, Dirk Sutter, Zsuzsanna Major, Thomas Metzger, and Ferenc Krausz. Third-generation femtosecond technology. *Optica*, 1(1):45–63, Jul 2014.

[27] Liang Feng, Ye-Long Xu, William S. Fegadolli, Ming-Hui Lu, José E. B. Oliveira, Vilson R. Almeida, Yan-Feng Chen, and Axel Scherer. Experimental demonstration of a unidirectional reflectionless parity-time metamaterial at optical frequencies. *Nat. Mater.*, 12(2):108–113, Feb 2013.

[28] Marco P. Fischer, Nicolò Maccaferri, Kevin Gallacher, Jacopo Frigerio, Giovanni Pellegrini, Douglas J. Paul, Giovanni Isella, Alfred Leitenstorfer, Paolo Biagioni, and Daniele Brida. Field-resolved detection of the temporal response of a single plasmonic antenna in the mid-infrared. *Optica*, 8(6):898–903, Jun 2021.

[29] Noah Flemens, Peter Krogen, Haim Suchowski, Houkun Liang, Kyung-Han Hong, Franz X. Kärtner, and Jeffrey Moses. Single-cycle or arbitrarily shaped octave-spanning mid-infrared pulses: Intrinsic and extrinsic pulse shaping in adiabatic frequency conversion. In *High-Brightness Sources and Light-driven Interactions*, page MW2C.7. Optica Publishing Group, 2018.

[30] Noah Flemens and Jeffrey Moses. Hermitian nonlinear wave mixing controlled by a pt-symmetric phase transition. arXiv preprint arXiv:2205.02922 [physics.app-ph], 2022.

[31] Noah Flemens, Nicolas Swenson, and Jeffrey Moses. Efficient parametric amplification via simultaneous second harmonic generation. *Opt. Express*, 29(19):30590–30609, Sep 2021.

[32] Yuxi Fu, Katsumi Midorikawa, and Eiji J. Takahashi. Towards a petawatt-class few-cycle infrared laser system via dual-chirped optical parametric amplification. *Scientific Reports*, 8(1):7692, May 2018.

[33] J. A. Fülöp, Z. Major, B. Horváth, F. Tavella, A. Baltuška, and F. Krausz. Shaping of picosecond pulses for pumping optical parametric amplification. *Appl. Phys. B*, 87:79–84, 2007.

[34] S. N. Ghosh and Y. D. Chong. Exceptional points and asymmetric mode conversion in quasi-guided dual-mode optical waveguides. *Sci. Rep.*, 6(19837):1–7, Apr 2016.

[35] J. A. Giordmaine. Mixing of light beams in crystals. *Phys. Rev. Lett.*, 8:19–20, Jan 1962.

[36] D. Heberle, N. Flemens, P. Lassonde, A. Leblanc, F. Légaré, and J. Moses. Self-dispersion-managed octave-spanning adiabatic frequency converter. in Conference on Lasers and Electro-Optics, OSA Technical Digest (Optica, 2022), paper STh4E.2.

[37] C. Heese, C. R. Phillips, L. Gallmann, M. M. Fejer, and U. Keller. Ultra-broadband, highly flexible amplifier for ultrashort midinfrared laser pulses based on aperiodically poled mg:linbo3. *Opt. Lett.*, 35(14):2340–2342, Jul 2010.

[38] C. Heese, C. R. Phillips, B. W. Mayer, L. Gallmann, M. M. Fejer, and U. Keller. 75 mw few-cycle mid-infrared pulses from a collinear apodized appln-based opcpa. *Opt. Express*, 20(24):26888–26894, Nov 2012.

[39] Hossein Hodaei, Absar U. Hassan, Steffen Wittek, Hipolito Garcia-Gracia, Ramy El-Ganainy, Demetrios N. Christodoulides, and Mercedeh Khajavikhan. Enhanced sensitivity at higher-order exceptional points. *Nature*, 548(7666):187–191, Aug 2017.

[40] Hossein Hodaei, Mohammad-Ali Miri, Matthias Heinrich, Demetrios N. Christodoulides, and Mercedeh Khajavikhan. Parity-time–symmetric microring lasers. *Science*, 346(6212):975–978, Nov 2014.

[41] Yue Jiang, Yefeng Mei, Ying Zuo, Yanhua Zhai, Jensen Li, Jianming Wen, and Shengwang Du. Anti-parity-time symmetric optical four-wave mixing in cold atoms. *Phys. Rev. Lett.*, 123:193604, Nov 2019.

[42] Tolga Kartaloğlu, Z. Gürkan Figen, and Orhan Aytür. Simultaneous phase matching of optical parametric oscillation and second-harmonic generation in aperiodically poled lithium niobate. *J. Opt. Soc. Am. B*, 20(2):343–350, Feb 2003.

[43] V. Kemlin, B. Boulanger, V. Petrov, P. Segonds, B. Ménaert, P. G. Schunneman, and K. T. Zawilski. Nonlinear, dispersive, and phase-matching properties of the new chalcopyrite cdsip2 [invited]. *Opt. Mater. Express*, 1:1292–1300, 2011.

[44] J. B. Khurgin, Y. Sebbag, E. Edrei, R. Zektzer, K. Shastri, U. Levy, and F. Monticone. Emulating exceptional-point encirclements using imperfect (leaky) photonic components: asymmetric mode-switching and omnipolarizer action. *Optica*, 8(4):563–569, Apr 2021.

[45] R. H. Kingston. Parametric amplification and oscillation at optical frequencies. *Proc. IRE*, 50:472–474, 1962.

[46] D. A. Kleinman. Nonlinear dielectric polarization in optical media. *Phys. Rev.*, 126:1977–1979, Jun 1962.

[47] P. Krogen, H. Suchowski, H. Liang, N. Flemens, K.-H. Hong, F. X. Kärtner, and J. Moses. Generation and multi-octave shaping of mid-infrared intense single-cycle pulses. *Nat Photonics*, 11:222–226, 2017.

[48] Peter Krogen, Haim Suchowski, Houkun Liang, Noah Flemens, Kyung-Han Hong, Franz X. Kärtner, and Jeffrey Moses. Generation and multi-octave shaping of mid-infrared intense single-cycle pulses. *Nat. Photonics*, 11(4):222–226, April 2017.

[49] Norman M. Kroll. Parametric amplification in spatially extended media and application to the design of tuneable oscillators at optical frequencies. *Phys. Rev.*, 127:1207–1211, Aug 1962.

[50] Yu-Hung Lai, Yu-Kun Lu, Myoung-Gyun Suh, Zhiquan Yuan, and Kerry Vahala. Observation of the exceptional-point-enhanced Sagnac effect. *Nature*, 576(7785):65–69, Dec 2019.

[51] W. Langbein. No exceptional precision of exceptional-point sensors. *Phys. Rev. A*, 98(2):023805, Aug 2018.

[52] F. Langer, C. P. Schmid, S. Schlauderer, M. Gmitra, J. Fabian, P. Nagler, C. Schüller, T. Korn, P. G. Hawkins, J. T. Steiner, U. Huttner, S. W. Koch, M. Kira, and R. Huber. Lightwave valleytronics in a monolayer of tungsten diselenide. *Nature*, 557(7703):76–80, May 2018.

[53] Hoi-Kwan Lau and Aashish A. Clerk. Fundamental limits and non-reciprocal approaches in non-Hermitian quantum sensing. *Nat. Commun.*, 9(4320):1–13, Nov 2018.

[54] Adrien Leblanc, Adrien Longa, Mayank Kumar, Antoine Laramée, Charles Dansereau, Heide Ibrahim, Philippe Lassonde, and François Légaré. Temporal characterization of two-octave infrared pulses by frequency resolved optical switching. *Journal of Physics: Photonics*, 3(4):045002, aug 2021.

[55] Y. Li, H. Zhong, J. Yang, S. Wang, and D. Fan. Versatile backconversion-inhibited broadband optical parametric amplification based on an idler-separated qpm configuration. *Opt. Lett.*, 42:2806–2809, 2017.

[56] H. Liang, P. Krogen, Z. Wang, H. Park, T. Kroh, K. Zawilski, P. Schunemann, J. Moses, L. F. DiMauro, F. X. Kartner, and K.-H. Hong. High-energy mid-infrared sub-cycle pulse synthesis from a parametric amplifier. *Nat. Commun.*, 8:141, 2017.

[57] Zin Lin, Hamidreza Ramezani, Toni Eichelkraut, Tsampikos Kottos, Hui Cao, and Demetrios N. Christodoulides. Unidirectional Invisibility Induced by $\mathcal{PT}$-Symmetric Periodic Structures. *Phys. Rev. Lett.*, 106(21):213901, May 2011.

[58] Zhao-Wei Liu, Yan Du, Jun Liao, Shi-Ning Zhu, Yong-Yuan Zhu, Yi-Qiang Qin, Hui-Tian Wang, Jing-Liang He, Chao Zhang, and Nai-Ben Ming. Engineering of a dual-periodic optical superlattice used in a coupled optical parametric interaction. *J. Opt. Soc. Am. B*, 19(7):1676–1684, Jul 2002.

[59] Adrien Longa, Mayank Kumar, Philippe Lassonde, Heide Ibrahim, Francois Legare, and Adrien Leblanc. Spectral phase sensitivity of frequency resolved optical switching for broadband ir pulse characterization. *Opt. Express*, 30(5):7968–7975, Feb 2022.

[60] J. Ma, J. Wang, P. Yuan, G. Xie, K. Xiong, Y. Tu, X. Tu, E. Shi, Y. Zheng, and L. Qian. Quasi-parametric amplification of chirped pulses based on a sm3+-doped yttrium calcium oxyborate crystal. *Optica*, 2:1006–1009, 2015.

[61] Jingui Ma, Jing Wang, Bingjie Zhou, Peng Yuan, Guoqiang Xie, Kainan Xiong, Yanqing Zheng, Heyuan Zhu, and Liejia Qian. Broadband, efficient, and robust quasi-parametric chirped-pulse amplification. *Opt. Express*, 25(21):25149–25164, Oct 2017.

[62] Cristian Manzoni, Oliver D. Mücke, Giovanni Cirmi, Shaobo Fang, Jeffrey Moses, Shu-Wei Huang, Kyung-Han Hong, Giulio Cerullo, and Franz X. Kärtner. Coherent pulse synthesis: towards sub-cycle optical waveforms. *Laser & Photonics Reviews*, 9(2):129–171, 2015.

[63] Cristian Manzoni, Oliver D. Mücke, Giovanni Cirmi, Shaobo Fang, Jeffrey Moses, Shu-Wei Huang, Kyung-Han Hong, Giulio Cerullo, and Franz X. Kärtner. Coherent pulse synthesis: towards sub-cycle optical waveforms. *Laser & Photonics Reviews*, 9(2):129–171, 2015.

[64] Peleg Margules, Jeffrey Moses, Haim Suchowski, and Gil Porat. Ultrafast adiabatic frequency conversion. *Journal of Physics: Photonics*, 3(2):022011, apr 2021.

[65] Peleg Margules, Jeffrey Moses, Haim Suchowski, and Gil Porat. Ultrafast adiabatic frequency conversion. *Journal of Physics: Photonics*, 3(2):022011, apr 2021.

[66] Andrey Markov, Anna Mazhorova, Holger Breitenborn, Andrew Bruhacs, Matteo Clerici, Daniele Modotto, Ottavia Jedrkiewicz, Paolo di Trapani, Arkady Major, François Vidal, and Roberto Morandotti. Broadband and efficient adiabatic three-wave-mixing in a temperature-controlled bulk crystal. *Opt. Express*, 26(4):4448–4458, Feb 2018.

[67] B. W. Mayer, C. R. Phillips, L. Gallmann, and U. Keller. Mid-infrared pulse generation via achromatic quasi-phase-matched opcpa. *Opt. Express*, 22(17):20798–20808, Aug 2014.

[68] Mohammad-Ali Miri and Andrea Alù. Nonlinearity-induced PT-symmetry without material gain. *New J. Phys.*, 18(6):065001, May 2016.

[69] G V Mironov and N N Filonenko. Optical inhomogeneity of nonlinear crystals and maximum efficiencies of parametric frequency amplifiers pumped by beams with inhomogeneous transverse intensity distributions. *Sov. J. Quantum Electron.*, 12(6):723–727, jun 1982.

[70] J. Moses and S.-W. Huang. Conformal profile theory for performance scaling of ultrabroadband optical parametric chirped pulse amplification. *J. Opt. Soc. Am. B*, 28:812–831, 2011.

[71] J. Moses, H. Suchowski, and F. X. Kärtner. Fully efficient adiabatic frequency conversion of broadband ti:sapphire oscillator pulses. *Opt Lett.*, 37:1589–1591, 2012.

[72] Gerard A. Mourou, Toshiki Tajima, and Sergei V. Bulanov. Optics in the relativistic regime. *Rev. Mod. Phys.*, 78:309–371, Apr 2006.

[73] A. H. Norton and C. M. de Sterke. Optimal poling of nonlinear photonic crystals for frequency conversion. *Opt Lett.*, 28:188–190, 2003.

[74] Ş K. Özdemir, S. Rotter, F. Nori, and L. Yang. Parity–time symmetry and exceptional points in photonics. *Nat. Mater.*, 18(8):783–798, Aug 2019.

[75] Midya Parto, Yuzhou G. N. Liu, Babak Bahari, Mercedeh Khajavikhan, and Demetrios N. Christodoulides. Non-hermitian and topological photonics: optics at an exceptional point. *Nanophotonics*, 10(1):403–423, 2021.

[76] C. R. Phillips and M. M. Fejer. Efficiency and phase of optical parametric amplification in chirped quasi-phase-matched gratings. *Opt Lett.*, 35:3093–3095, 2010.

[77] R. Piccoli, J. M. Brown, Y.-G. Jeong, A. Rovere, L. Zanotto, M. B. Gaarde, F. Légaré, A. Couairon, J. C. Travers, R. Morandotti, B. E. Schmidt, and L. Razzari. Intense few-cycle visible pulses directly generated via nonlinear fibre mode mixing. *Nat. Photonics*, 15(12):884–889, December 2021.

[78] Gil Porat and Ady Arie. Efficient, broadband, and robust frequency conversion by fully nonlinear adiabatic three-wave mixing. *J. Opt. Soc. Am. B*, 30(5):1342–1351, 2013.

[79] A. Bahabad R. Lifshitz, A. Arie. Photonic quasicrystals for nonlinear optical frequency conversion. *Phys. Rev. Lett.*, 95:133901, Sep 2005.

[80] Richard H. Rand. *Lecture Notes on Nonlinear Vibrations*, chapter 2. 2012. URL: https://hdl.handle.net/1813/28989.

[81] Arkadev Roy, Saman Jahani, Qiushi Guo, Avik Dutt, Shanhui Fan, Mohammad-Ali Miri, and Alireza Marandi. Nondissipative non-hermitian dynamics and exceptional points in coupled optical parametric oscillators. *Optica*, 8(3):415–421, Mar 2021.

[82] Arkadev Roy, Saman Jahani, Carsten Langrock, Martin Fejer, and Alireza Marandi. Spectral phase transitions in optical parametric oscillators. *Nat. Commun.*, 12(835):1–9, February 2021.

[83] Eyal Rozenberg and Ady Arie. Broadband and robust adiabatic second-harmonic generation by a temperature gradient in birefringently phase-matched lithium triborate crystal. *Opt. Lett.*, 44(13):3358–3361, Jul 2019.

[84] Solomon M. Saltiel, Andrey A. Sukhorukov, and Yuri S. Kivshar. Chapter 1 - multistep parametric processes in nonlinear optics. In E. Wolf, editor, *Progress in Optics*, volume 47, pages 1 – 73. Elsevier, 2005.

[85] D. Sánchez, M. Hemmer, M. Baudisch, K. Zawilski, P. Schunemann, H. Hoogland, R. Holzwarth, and J. Biegert. Broadband mid-ir frequency comb with $CdSiP_2$ and $AgGaS_2$ from an Er,Tm:Ho fiber laser. *Opt. Lett.*, 39(24):6883–6886, Dec 2014.

[86] Bruno E. Schmidt, Nicolas Thiré, Maxime Boivin, Antoine Laramée, François Poitras, Guy Lebrun, Tsuneyuki Ozaki, Heide Ibrahim, and François Légaré. Frequency domain optical parametric amplification. *Nat. Commun.*, 5(3643):1–8, May 2014.

[87] Aleem M. Siddiqui, Kyung-Han Hong, Jeffrey Moses, and Franz X. Kärtner. Bandwidth extension and conversion efficiency improvements beyond phase matching limitations using cavity-enhanced opcpa. *Opt. Express*, 29(7):9907–9926, Mar 2021.

[88] Aleem M. Siddiqui, Jeffrey Moses, Kyung-Han Hong, Chien-Jen Lai, and Franz X. Kärtner. Performance scaling via passive pulse shaping in cavity-enhanced optical parametric chirped-pulse amplification. *Opt. Lett.*, 35(12):1929–1931, Jun 2010.

[89] Haim Suchowski, Dan Oron, Ady Arie, and Yaron Silberberg. Geometrical representation of sum frequency generation and adiabatic frequency conversion. *Phys. Rev. A*, 78:063821, Dec 2008.

[90] Haim Suchowski, Gil Porat, and Ady Arie. Adiabatic processes in frequency conversion. *Laser & Photonics Rev.*, 8(3):333–367, 2014.

[91] Haim Suchowski, Gil Porat, and Ady Arie. Adiabatic processes in frequency conversion. *Laser & Photonics Rev.*, 8(3):333–367, 2014.

[92] Andreas Vaupel, Nathan Bodnar, Benjamin Webb, Lawrence Shah, and Martin C. Richardson. Concepts, performance review, and prospects of table-top, few-cycle optical parametric chirped-pulse amplification. *Opt. Eng.*, 53(5):1 – 12, 2013.

[93] Yu-Xin Wang and A. A. Clerk. Non-hermitian dynamics without dissipation in quantum systems. *Phys. Rev. A*, 99:063834, Jun 2019.

[94] S. Witte and K. S. E. Eikema. Ultrafast optical parametric chirped-pulse amplification. *IEEE J. Sel. Top. Quantum Electron.*, 18(1):296–307, 2012.

[95] Fangxing Zhang, Yaming Feng, Xianfeng Chen, Li Ge, and Wenjie Wan. Synthetic anti-pt symmetry in a single microcavity. *Phys. Rev. Lett.*, 124:053901, Feb 2020.

[96] Q. Zhong, A. Ahmed, J. I. Dadap, R. M. Osgood, and R. El-Ganainy. Parametric amplification in quasi-pt symmetric coupled waveguide structures. *New J. Phys.*, 18:125006, 2016.